Supplementary Information

Multidentate Silane Bridging for Stable and Efficient Perovskite–Organic Tandem Solar Cells

Dong Zhang,[a] Baoze Liu,[a] Xue Wang,[ab] Qi Liu,[c] Danpeng Gao,*[a] Xianglang Sun,*[a] Xin Wu,[a] Zexin Yu,[a] Chunlei Zhang,[a] Ning Wang,[a] Yan Wang,[a] Nikhil Kalasariya,[d] Francesco Vanin,[a] Weidong Tian,[a] Shuai Li,[a] Jianqiu Gong,[a] Lina Wang,[a] Yang Bai,[e] Shuang Xiao,[f] Bo Li,[g] Martin Stolterfoht,[d] Xiao Cheng Zeng,*[c] Shangfeng Yang*[b] and Zonglong Zhu*[ahi]

[a]*Department of Chemistry, City University of Hong Kong, Hong Kong SAR, P. R. China*

[b]*Department of Materials Science and Engineering, University of Science and Technology of China, Hefei, Anhui, P. R. China*

[c]*Department of Materials Science & Engineering, City University of Hong Kong, Hong Kong SAR, P. R. China*

[d]*Department of Electronic Engineering, The Chinese University of Hong Kong, Hong Kong SAR, P. R. China*

[e]*School of Materials Science and Engineering, Beijing Institute of Technology, Beijing, P. R. China*

[f] *Center for Advanced Material Diagnostic Technology and College of Engineering Physics, Shenzhen Technology University, Shenzhen, Guangdong, P. R. China*

[g]*Department of Materials Science & Engineering, Central South University, Changsha, Hunan, P. R. China*

[h]*Hong Kong Institute for Clean Energy, City University of Hong Kong, Hong Kong SAR, P. R. China*

[i]*City University of Hong Kong Shenzhen Research Institute, Shenzhen, Guangdong, P. R. China*

*Corresponding authors. E-mail: zonglzhu@cityu.edu.hk; sfyang@ustc.edu.cn; xzeng26@cityu.edu.hk; sxl@hust.edu.cn; dp.gao@cityu.edu.hk

Experimental Methods

Materials

Formamidinium iodide (FAI) was purchased from Dysol. Lead iodide (PbI_2), lead bromide ($PbBr_2$), Me-2PACz, and 2PACz were purchased from TCI. Cesium iodide (CsI), cesium bromide (CsBr), formamidinium bromide (FABr), and C_{60}, bathocuproine (BCP, purity of 99.9%) were purchased from Xi'an Yuri Solar Corporation. N, N-Dimethylformamide (DMF), dimethyl sulfoxide (DMSO), chlorobenzene (CB), methanol (MT), and isopropanol (IPA) were purchased from *J&K* Scientific. Chloroform (CF) and MoO_x were purchased from Sigma Aldrich. PM6 and PM7 were purchased from Volt-Amp Optoelectronics Tech. Co., Ltd. Y6, $PC_{61}BM$ were purchased from Solarmer Materials, Inc. NiO_x was purchased from Advanced Election Technology Co., Ltd.

Fabrication of 1.82 eV wide bandgap (WBG) perovskite solar cells

The perovskite precursor solution was prepared by mixing FAI, FABr, CsI, CsBr, $PbBr_2$, and PbI_2 in DMF/DMSO (4:1) with a 0.9 M concentration. The molar ratios of FA^+/Cs^+ and I^-/Br^- were kept at 80:20 and 55:45 to form the composition $Cs_{0.2}FA_{0.8}Pb(I_{0.55}Br_{0.45})_3$, respectively. The perovskite solution was stirred at 45 ℃ for 3 hours. Afterward, PEAI (2mg/ml) was added to the solution before use. Glass/ITO substrates (8 Ω sq^{-1}) were sequentially cleaned by sonication with detergent for 30 min, deionized water, acetone, isopropyl alcohol, and ethanol for 20 min, respectively. Then, the glass/ITO substrates were dried at 70 °C in an oven. Before use, the substrates were treated with UV ozone for 30 min. The NiO_x solution (10 mg/mL) was filtered with a hydrophilic PTFE filter (0.22 μm) and then spin-coated on a glass/ITO substrate at 4,000 rpm for 30 s, followed by annealing at 130 °C for 10 min. Then, the substrates were transferred to the N_2 glovebox and annealed for an additional 5 minutes at 100 ℃. The solution of Me-2PACz (0.3 mg/ml in methanol) was spin-coated onto the glass/ITO/NiO_x substrate at 4,000 rpm for 30 s, followed by annealing at 100 °C for 10 min in a nitrogen atmosphere. The substrates were cooled down to room temperature before depositing the perovskite layer. The perovskite solution was spin-coated onto glass/ITO/NiO_x/Me-2PACz substrate at 2,000 rpm for

10s and 6,000 rpm for 40 s, and 200 µl CB was dripped onto the center of the film at 20 s before the end of the spin coating, followed by annealing on a hotplate at 100°C for 15 min. The diluted FPTS solution (1:5 in IPA) was rapidly dropped onto the perovskite substrate and spin-coated at 5,000 rpm for 30 s. The film was then vacuum annealed in a glove box transfer chamber (~7.5×10^{-2} torr) to form a FPTS film, or the film was annealed on a hot plate at 100 °C for 10 minutes to obtain a poly-FPTS film. Then, 25 nm C_{60}, 6 nm BCP, and 100 nm silver were sequentially thermally evaporated under high vacuum (< 4×10^{-6} torr). The device area was characterized as 0.034 cm^2 by a metal shadow mask.

Fabrication of 1.53 eV perovskite solar cells

For perovskite precursor preparation, 1.59 M perovskite precursor solution was prepared by mixing 20.7 mg of CsI, 25.3 mg of MAI, 238.1 mg of FAI and 791.6 mg of PbI_2 (8% of excess PbI_2 was needed to improve the device performance) in 1 ml DMF/DMSO (4:1 in volume) mixed solvent with a chemical formula of $Cs_{0.05}FA_{0.85}MA_{0.1}PbI_3$ to form a 1.53 eV perovskite. Then 10 mol% MACl was added to the perovskite precursor solution and stirred for 15 mins. After 30 min UV ozone, the NiO_x solution (10 mg/mL) was filtered with a hydrophilic PTFE filter (0.22 µm) and then spin-coated on a glass/ITO substrate at 4,000 rpm for 30 s, followed by annealing at 130 °C for 10 min. Then, the substrates were transferred to the N_2 glovebox and annealed for an additional 5 minutes at 100 ℃. The solution of Me-4PACz (0.3 mg/ml in methanol) was spin-coated onto the glass/ITO/NiO_x substrate at 4,000 rpm for 30 s, followed by annealing at 100 °C for 10 min in a nitrogen atmosphere. The substrates were cooled down to room temperature before depositing the perovskite layer. Next, 100 µl of the perovskite solution was dropped onto the ITO substrate, allowed to settle undisturbed for a duration of 10 s, and then spin-coated at 1,000 r.p.m for 10 s, and then subsequently at 5,000 r.p.m. for 40 s. Chlorobenzene (300 µl) was dripped onto the centre of the film at 8 s before the end of spin-coating. The deposited perovskite films were subsequently annealed on a hotplate at 100 °C for 30 min and 120 °C for 10 min. For devices with surface passivation treatment, a diluted FPTS solution (1:5 in IPA) was quickly dropped onto the perovskite substrate and spin-coated at 5,000

rpm for 30 s, followed by annealing at 100 °C for 10 min. Finally, 30 nm C_{60} at a rate of 0.5 Å s^{-1}, 6 nm BCP at a rate of 0.2 Å s^{-1}, and 100 nm silver electrode at a rate of 1.0 Å s^{-1} were thermally evaporated, respectively, under high vacuum (< 4×10^{-6} torr).

Fabrication of 1.68 eV perovskite solar cells

A 1.4-M perovskite precursor solution ($FA_{0.8}MA_{0.15}Cs_{0.05}Pb(I_{0.78}Br_{0.22})_3$) was prepared by dissolving CsI (18.2 mg), MABr (23.6 mg), FAI (192.6 mg), PbI_2 (536 mg, 10% excess), and $PbBr_2$ (131 mg) in 1 mL of mixed DMF: DMSO (4:1, v/v) solvent. After 30 min UV ozone, the NiO_x solution (10 mg/mL) was filtered with a hydrophilic PTFE filter (0.22 μm) and then spin-coated on a glass/ITO substrate at 4,000 rpm for 30 s, followed by annealing at 130 °C for 10 min. Then, the substrates were transferred to the N_2 glovebox and annealed for an additional 5 minutes at 100 ℃. The solution of Me-4PACz (0.3 mg/ml in methanol) was spin-coated onto the glass/ITO/NiO_x substrate at 4,000 rpm for 30 s, followed by annealing at 100 °C for 10 min in a nitrogen atmosphere. The substrates were cooled down to room temperature before depositing the perovskite layer. Next, 60 μL of perovskite precursor was spin-coated at 1,000 rpm for 10 s and then at 4,000 rpm for 30 s, with 150 μL of CB dripped onto the center of the substrate at 5 s before the spin-coating process ended. This was followed by annealing at 100°C for 15 min in N_2. For devices with surface passivation treatment, a diluted FPTS solution (1:5 in IPA) was quickly dropped onto the perovskite substrate and spin-coated at 5,000 rpm for 30 s, followed by annealing at 100 °C for 10 min. Finally, 25 nm C_{60} at a rate of 0.5 Å s^{-1}, 6 nm BCP at a rate of 0.2 Å s^{-1}, and 100 nm silver electrode at a rate of 1.0 Å s^{-1} were thermally evaporated, respectively, under high vacuum (< 4×10^{-6} torr).

Fabrication of narrow bandgap (NBG) organic solar cells and tandem solar cells (TSCs)

A 10 nm layer of MoOx was thermally evaporated onto ITO in single-junction solar cells or onto ICLs in TSCs. Afterward, for TSCs, 40 μL 2PACz solution (0.3 mg/ml in IPA) was spin-coated at 4,000 rpm for 30 s, followed by annealing at 100 ℃ for 100 min. To form the quaternary bulk heterojunction (BHJ), PM6, PM7, Y6, and $PC_{61}BM$ with a weight ratio of

0.8:0.2:1.2:0.3 were dissolved in chloroform (polymer concentration 7.8 mg mL^{-1}) and stirred at 50 ℃ for 4 h. 0.5 vol% of 1-chloronaphthalene was added to the solution. Spin-coating was performed dynamically at 3,000 rpm for 30 s, followed by annealing at 100 ℃ for 5 min. Then, 10 nm C_{60}, 5 nm BCP, and 100 nm Ag were thermally evaporated sequentially under a high vacuum (< 4×10^{-6} Torr). Following the fabrication process of wide-E_g perovskite solar cells, after the thermal evaporation of 6 nm BCP, 0.5 nm Au, and 10 nm MoO_x were evaporated under high vacuum (< 4×10^{-6} Torr) to finish the preparation of the interconnecting layer. Then, the OPV subcells were finished using the same procedure as single-junction solar cells. For selected tandem cells, a 100 nm thick MgF_2 layer was thermally evaporated onto the back side of the glass substrate as an antireflection layer, under high vacuum (< 4×10^{-6} torr).

Photovoltaic performance characterization

The current-voltage (*J-V*) characteristics of photovoltaic devices were measured in an N_2-filled glovebox at room temperature using a xenon lamp solar simulator (Enlitech, SS-F5, Taiwan). The power of the light was calibrated to 100 mW cm^{-2} by a silicon control cell (with a KG2 filter). All the devices were measured using a Keithley 2400 source meter under a sweep mode of reverse scan (from 1.4 to -0.1 V) and forward scan (from -0.1 to 1.4 V) with the scan rate of 1 V s^{-1}, and the delay time was 10 ms. No preconditioning was needed before measurement. The stabilized power output was conducted by monitoring the stabilized current density output at the MPP bias (extracted from the reverse scan *J-V* curves). EQE and internal quantum efficiency (IQE) measurements were carried out using a QE-R EQE system (Enlitech, Taiwan).

Stability test

Operational stability was achieved by following the ISOS-L-1I and ISOS-L-2 procedures. For the ISOS-L-1I, the devices were tested in a N_2-filled glovebox. For ISOS-L-2 tests, the POTSCs were encapsulated (LT-U001, Luminescence Technology Corp.) with a cover glass (1.1 mm). The encapsulated POTSCs were operated under a 1-sun equivalent LED lamp in an N_2-filled

glovebox (with the contents of O_2 and H_2O <5 ppm). The POTSCs were biased at maximum power point (MPP) voltage, and the power output was tracked using a multi-potentiostat (CHI1040C, CH Instruments, Inc.). During the MPP test, the current density-voltage (*J-V)* curves of the devices were obtained every 12 hours to get the proper loads for the MPP. The devices were mounted on a hotplate for testing at 25 ℃, 45 ℃, 65 ℃, and 85 ℃. A thermometer regularly monitors the temperature of the devices. For the MPP tracking tests under illumination, the device was fixed at the MPP voltage (V_{mpp}), and the current density variation in the N_2 glovebox at RT was recorded without controlling the device temperature. For the light cycling stability tests, the encapsulated devices were kept at room temperature in air (24 ± 3 °C, 75 ± 5% RH), and the *J-V* curves were recorded at certain time intervals.

DFT calculation

The first-principles DFT simulations were performed with the Vienna Ab Initio Simulation Package (VASP 6.4)[1–3] to study the geometric and electronic structures of all the bare, FPTS, and poly-FPTS-treated $FAPb(I_{0.55}Br_{0.45})_3$ perovskite surface structures with (001) PbI_2 terminal, within or without any pre-set defects. Unless otherwise specified, the generalized gradient approximation exchange-correlation functional of Perdew-Burke-Ernzerhof (PBE)[3] was adopted in the DFT calculations. The electronic constituents are 2s 2p for C, N, O, and F, 3s 3p 3d for Si, 6s 5d for Pb, and 1s for H. For all the bare, FPTS and poly-FPTS-treated perovskite surface structures, we adopted a 2 × 2 × 1 k-point mesh for 2D vacuum surfaces, generated by the Monkhorst-Pack scheme. Considering the strong relativistic effect of the heavy element atoms like Pb, the spin-orbit coupling (SOC) effect was considered for all the calculations. The projector augmented wave (PAW) pseudopotentials with the cut-off energy of 600 eV were employed. Considering the van der Waals interaction between the hydrogen atoms and high-electronegativity groups, the PBE with the DFT-D3 dispersion correction of Grimme with zero-damping[4–6] was applied to optimize the geometric structures. During optimizing the geometries, all structures except the fixed bottom edge of perovskite adjacent to the vacuum were allowed to relax to ensure that each atom was in mechanical equilibrium without any residual force

larger than 10^{-4} eV/Å. A 25-Å vacuum layer was adopted on the surface structures so that the interaction between the fixed terminal layers can be neglected. Since the VASP 6.4 package cannot handle the charged vacuum structure well, all the defect-including surface structures were considered neutrally charged.

Characterizations and measurements

X-ray photoelectron spectroscopy (XPS) measurements were conducted via the AXIS Supra XPS system. The surface and cross-section morphology of the perovskite films were acquired by scanning electron microscopy (SEM) (QUATTROS, Thermal Fisher Scientific). The chamber was filled with high-purity nitrogen to minimize the influence of ambient conditions on the measurements. Steady-state PL and time-resolved PL were measured using an Edinburgh FLS980 system. The light was illuminated from the top surface of the perovskite film. For steady-state PL measurements, the excitation source was from a monochromated Xe lamp (peak wavelength at 520 nm with a line width of 2 nm). TRPL was measured using a Horiba Fluorolog-3 time-correlated single photon counting system; the samples were excited using a pulsed laser with a wavelength of 485 nm (11.7 mW cm^{-2}, 2 MHz, 5.83 nJ cm^{-2}). A PSC was used to adjust the laser intensity to a 1-sun equivalent intensity by obtaining a current density at 0 V that was approximately equal to its short-circuit current density (J_{SC}) under a standard solar simulator. Highly sensitive external quantum efficiency (EQE) was measured by an integrated system (PECT-600, Enlitech, Taiwan), where the photocurrent was amplified and modulated by a lock-in instrument. Temperature-dependent conductivity measurements for deriving the activation energy of ion migration (E_a) were conducted using an N_2 cryostat (Optistat DN-V, Oxford Instruments). The temperature was controlled by a cryogenic environment controller (Mercury iTC, Oxford Instruments). The active area and thickness sample specifications were set to 0.034 cm^2 and 400 nm for the Mott-Schottky measurement. The applied direct current voltage was set in the range of 0 to 2 V with 35 steps. The alternating current (AC) amplitude was kept constant at 70 mV, with the frequency scanned from 1 kHz to 100 kHz. ToF-SIMS was performed using ToF-SIMS M5 from IONTOF GmbH. Samples were

analysed in the dual-beam profiling mode. All profiles were conducted in the non-interlaced mode. Spectral data were acquired in the high mass-resolution mode. The primary ion for analysis was 30 keV Bi^{3+} 726 at 0.3 pA (with a Bi liquid metal ion source). This ion beam was applied over a 100 × 100 μm^2 area at the center of the sputter crater. The sputter ion was 10 keV Ar^+ at 120 nA (with an Ar electron impact ion source). A 300 × 300 μm^2 sputter crater was used.

Supplementary Figures

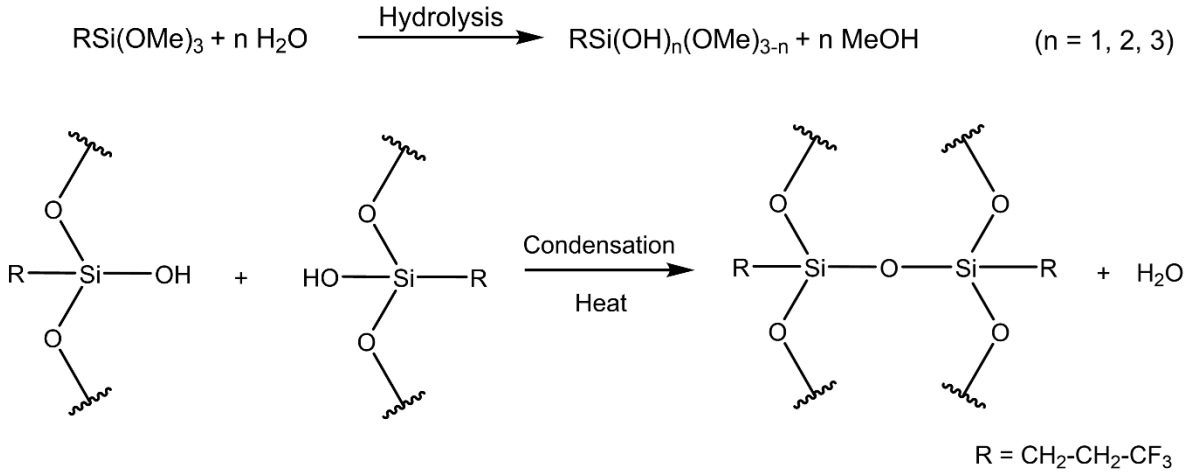

Figure S1. The reaction process of generating poly-FPTS from FPTS molecules.

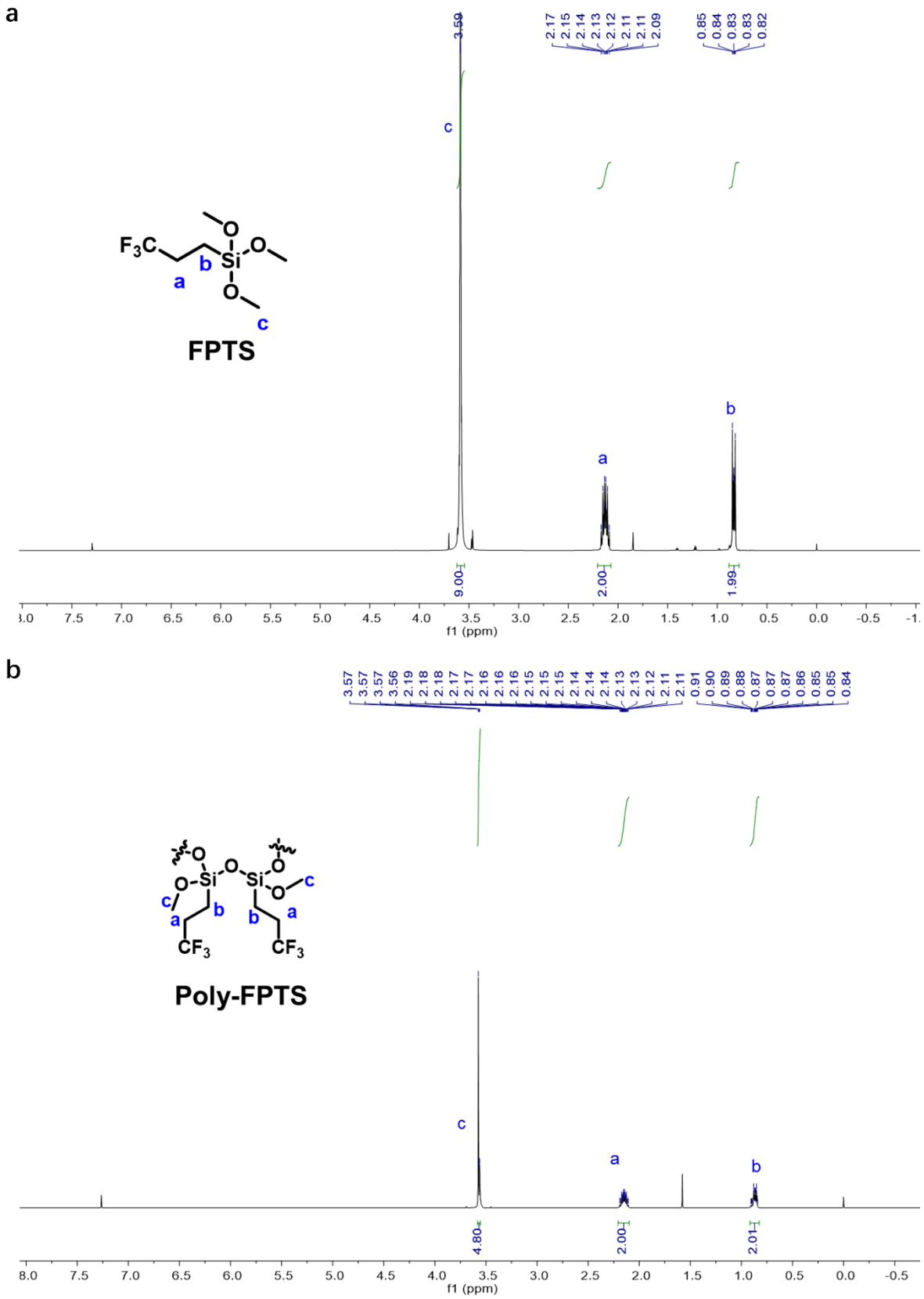

Figure S2. The ^{1}H-NMR spectra of FPTS before (**a**) and after (**b**) heating, conducted in chloroform-d.

Note: The structural evolution of 3-trifluoropropyltrimethoxysilane ($CF_3CH_2CH_2Si(OCH_3)_3$) in isopropanol (IPA) was investigated using ^1H NMR spectroscopy and its correlation with the reaction mechanism. Before heating, the spectrum showed a characteristic integral ratio of 9:2:2, corresponding to the three equivalent methoxy groups attached to silicon and the two methylene units on the trifluoropropyl chain. Upon heating in IPA, a new resonance peak attributable to the isopropoxy groups appeared, indicating a hydrolysis reaction in which the $Si\text{-}OCH_3$ groups were partially substituted by Si-OiPr. This process proceeded via nucleophilic attack of the electrophilic silicon center by the IPA, accompanied by the release of methanol, while the CF_3-propyl backbone remained unchanged.

After a period of heating, a significant decrease in the $Si\text{-}OCH_3$ signal was observed, with its integral value dropping from 9.00 to 4.80, while the methylene signal remained unchanged. This corresponds to the consumption of approximately 1.6 methoxy groups per silicon atom, representing a conversion of approximately 53% relative to the initial three alkoxy groups. This selective loss of alkoxy protons coincides with the partial hydrolysis of the Si-OR group by trace amounts of water, generating silanol (Si-OH) species, which subsequently undergo dehydration condensation to form Si-O-Si bonds. Therefore, the degree of methoxy consumption measured by NMR quantitatively supports a mechanism involving alcoholysis-assisted hydrolysis and subsequent partial siloxane crosslinking.

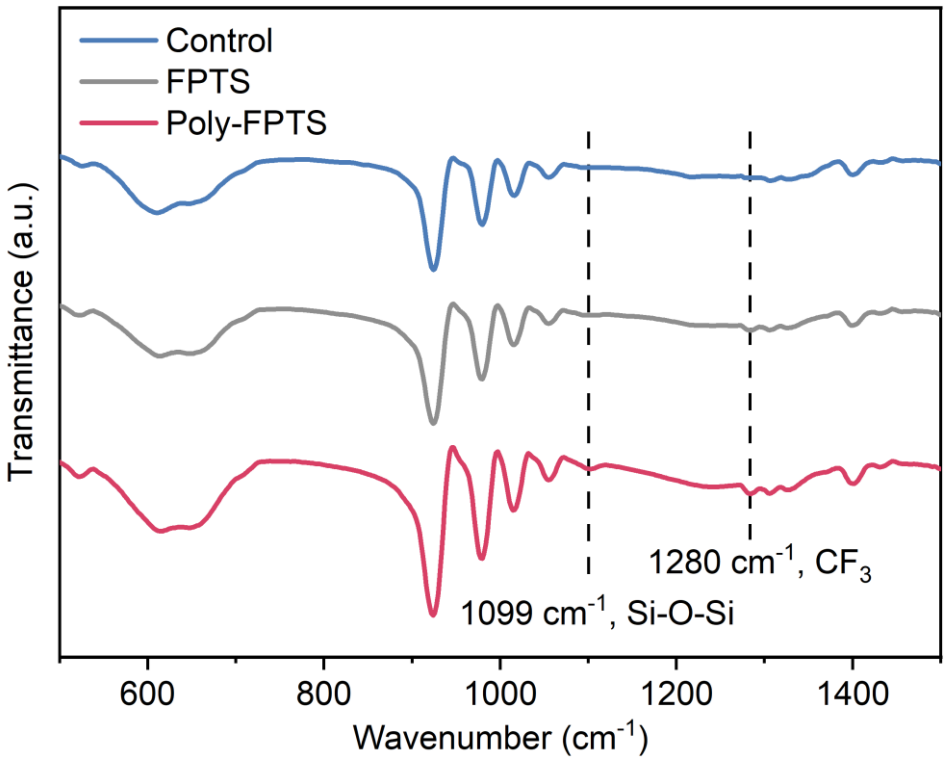

Figure S3. Fourier transform infrared (FTIR) spectra of untreated, FPTS and poly-FPTS treated perovskite films. Poly-FPTS and FPTS films are obtained by thermal annealing, and without thermal annealing after spin coating FPTS. The broad absorption peak at 1099 cm^{-1} from the FPTS-treated films is assigned to the Si-O-Si vibration,[7–9] indicating that coupling reactions occur with FPTS on the surface of the perovskite film.

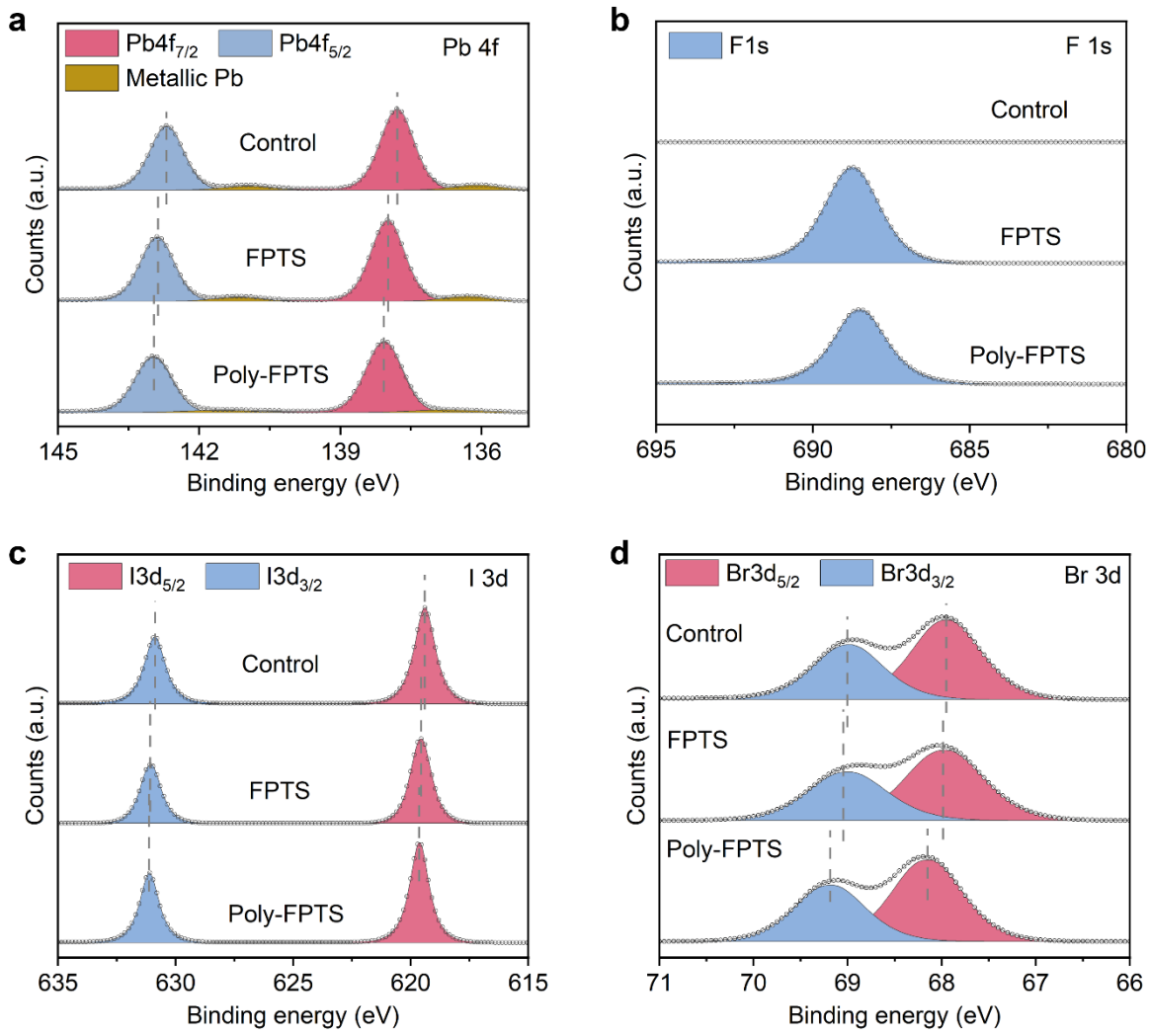

Figure S4. The X-ray photoelectron spectroscopy (XPS) spectra of F 1s, I 3d and Br 3d in untreated, FPTS-treated and poly-FPTS-treated perovskite films. All the XPS peak fittings were performed with Avantage software (Thermo Fisher). The background (Shirley) and peaks (Gauss–Lorentz type) were automatically fitted and optimized by the software.

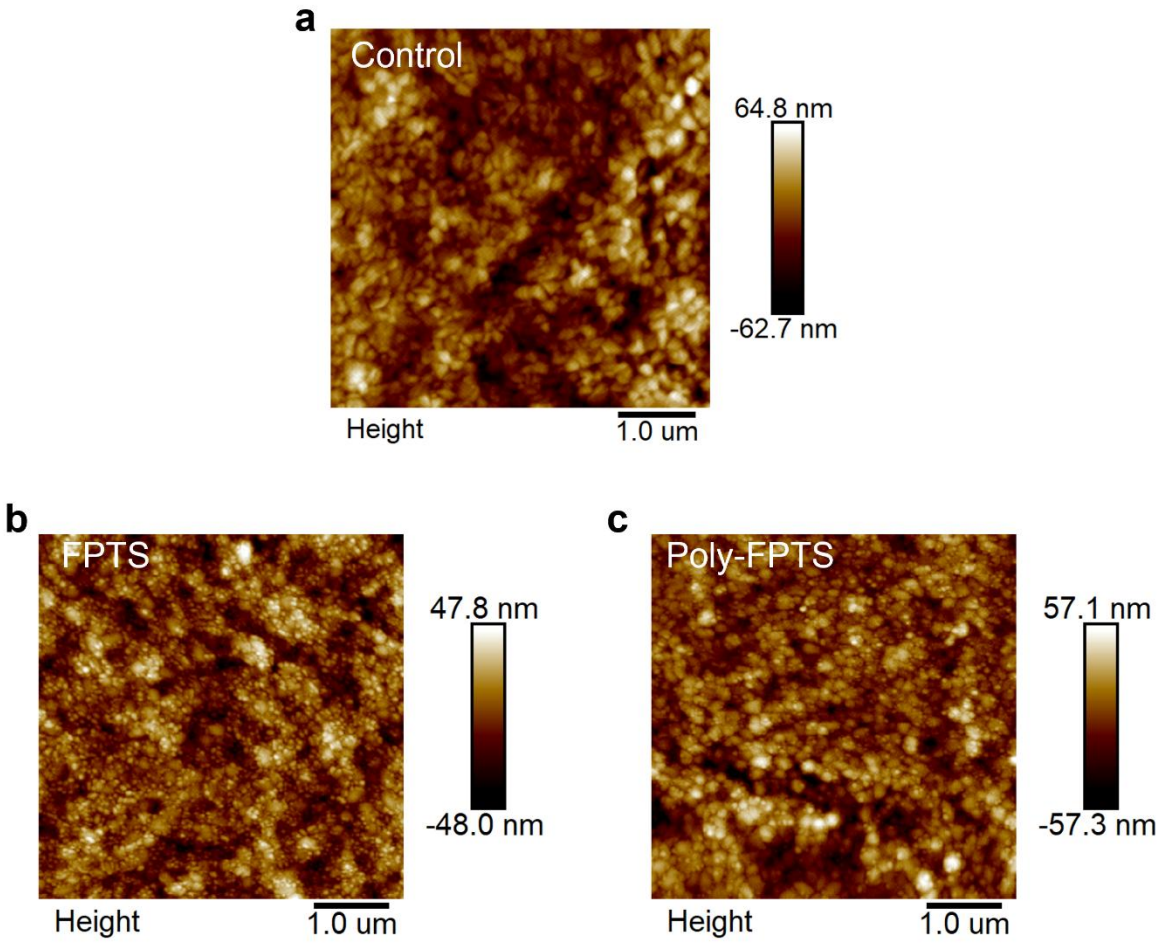

Figure S5. Atomic force microscopy (AFM) of untreated (**a**), FPTS-treated (**b**), and poly-FPTS-treated (**c**) films. The scale bar is 1 μm.

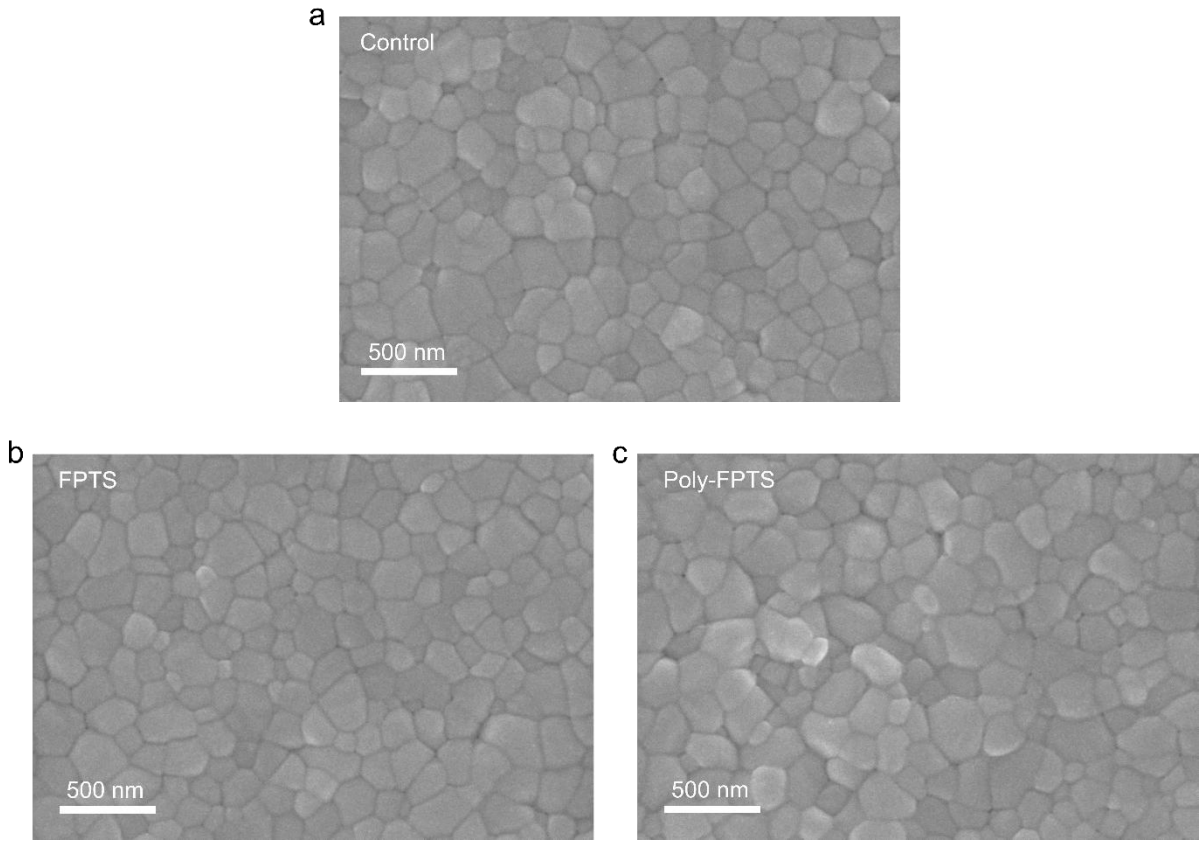

Figure S6. Scanning electron microscope (SEM) of untreated (**a**), FPTS-treated (**b**), and poly-FPTS-treated (**c**) perovskite films. The scale bar is 500 nm.

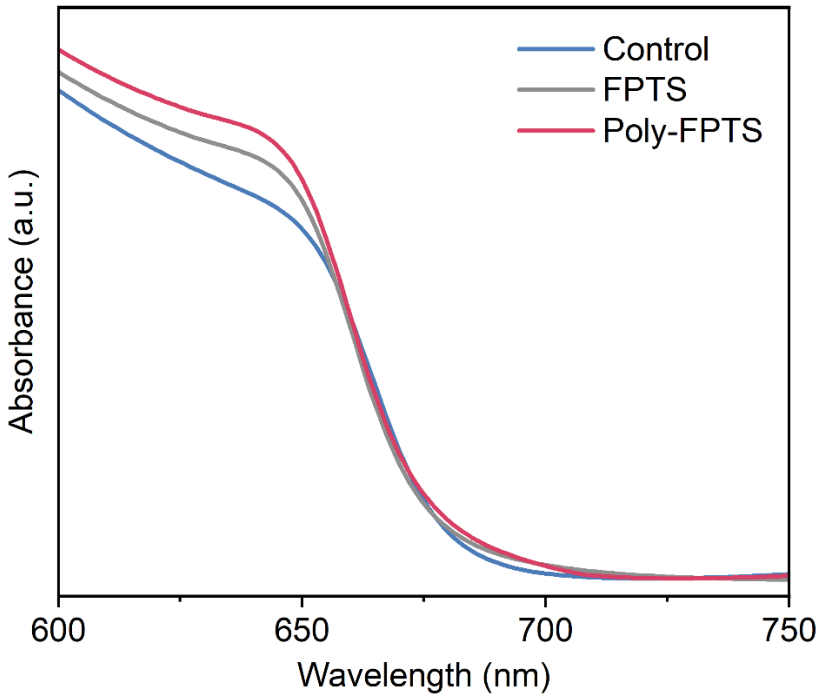

Figure S7. UV-vis spectra of untreated, FPTS-treated and poly-FPTS-treated perovskite films.

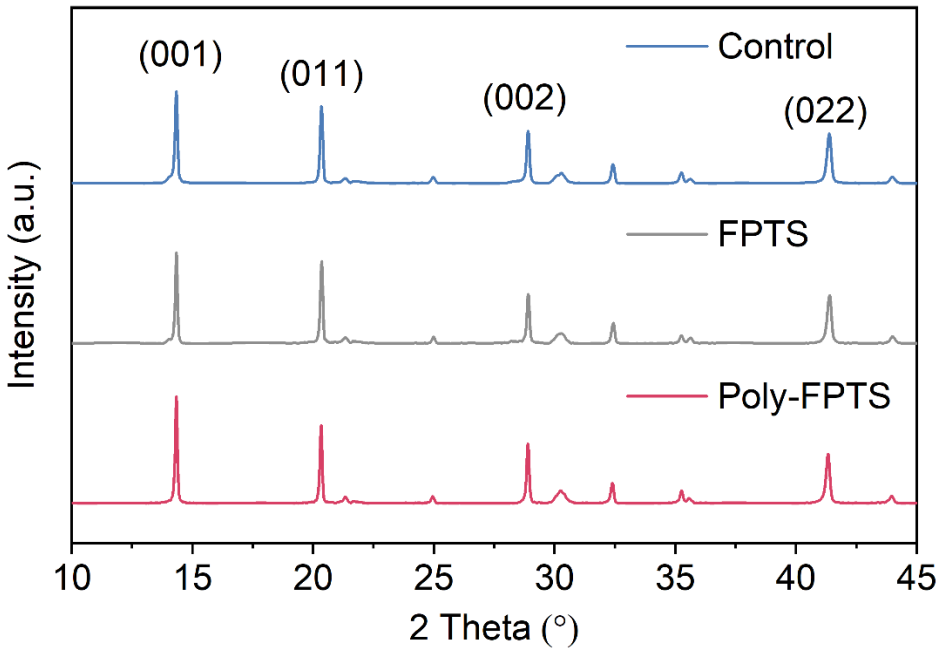

Figure S8. XRD patterns of untreated, FPTS-treated and poly-FPTS-treated perovskite films.

Note: All three samples exhibited the same diffraction peak positions and similar peak widths on characteristic perovskite crystal planes, such as (001), (011), (002). No additional diffraction peaks or significant peak shifts were observed, indicating that neither treatment altered the lattice parameters or inherent crystallinity of the perovskite layer.

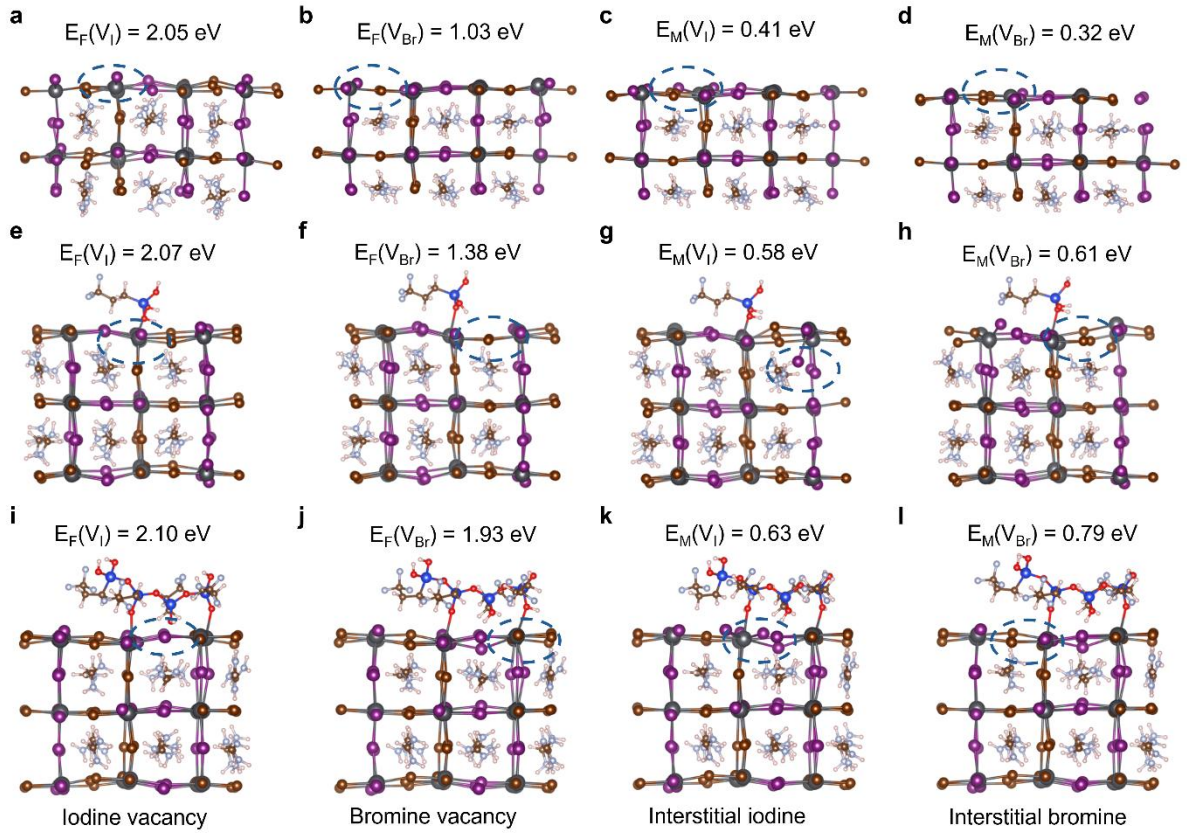

Figure S9. DFT calculated formation energy of iodine vacancy and bromine vacancy based on untreated (**a, b**), FPTS (**e, f**), and poly-FPTS treated (**i, j**) perovskites. DFT calculated migration energy of interstitial iodine and interstitial bromine based on untreated (**c, d**), FPTS (**g, h**), and poly-FPTS treated (**k, l**) perovskites.

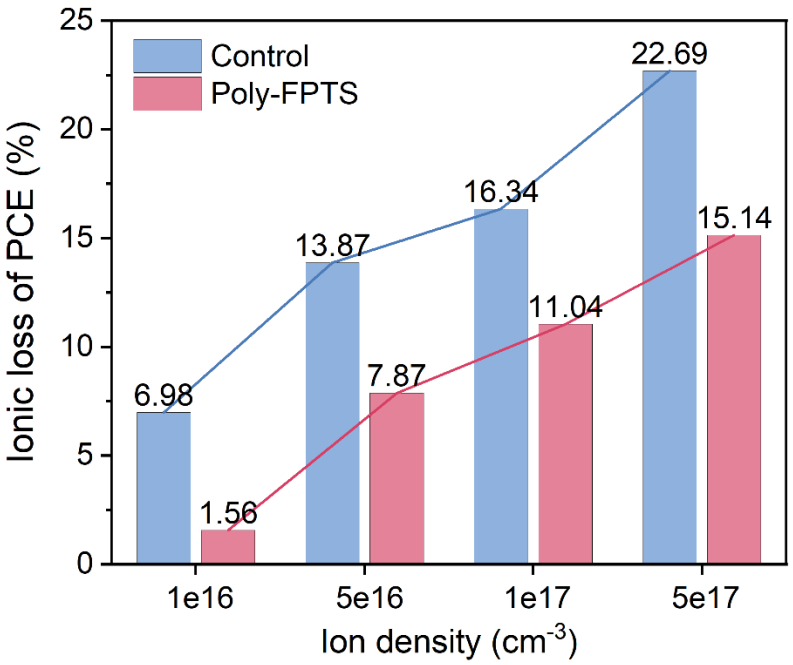

Figure S10. Simulated ionic loss of PCE versus ion density based on perovskite devices without and with poly-FPTS treatment.

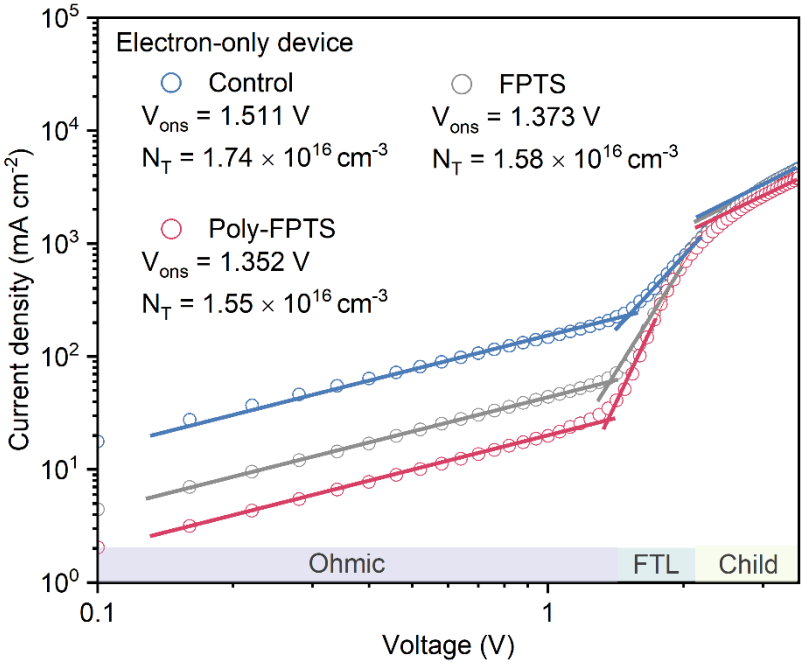

Figure S11. *J-V* curves of electron-only devices of untreated, FPTS-treated, and poly-FPTS-treated perovskite films, based on the structure of glass/ITO/SnO_x/perovskite (without and with poly-FPTS)/C_{60}/BCP/Ag.

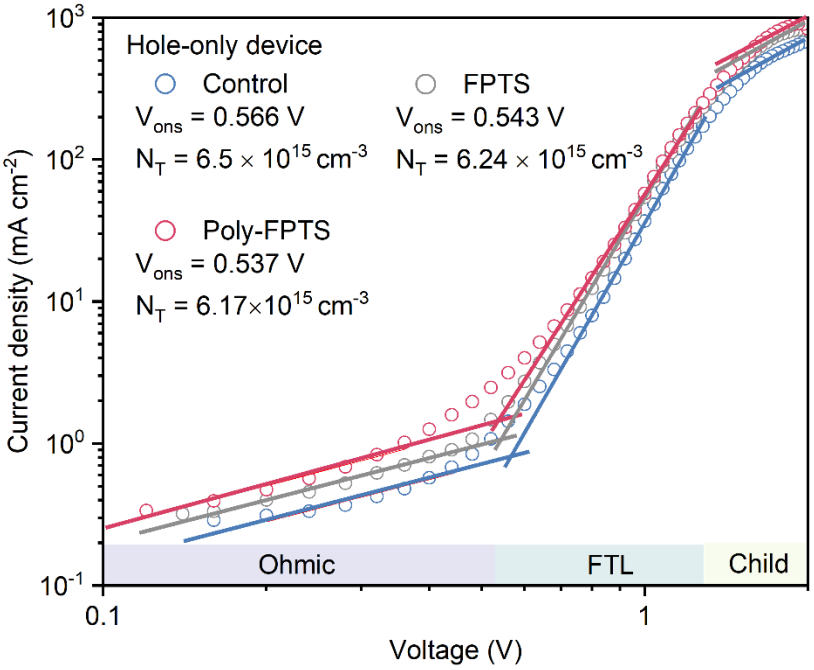

Figure S12. *J-V* curves of hole-only devices of untreated, FPTS-treated, and poly-FPTS-treated perovskite films, based on the structure of glass/ITO/NiO_x/Me-2PACz/perovskite (without and with poly-FPTS)/MoO_x/Ag.

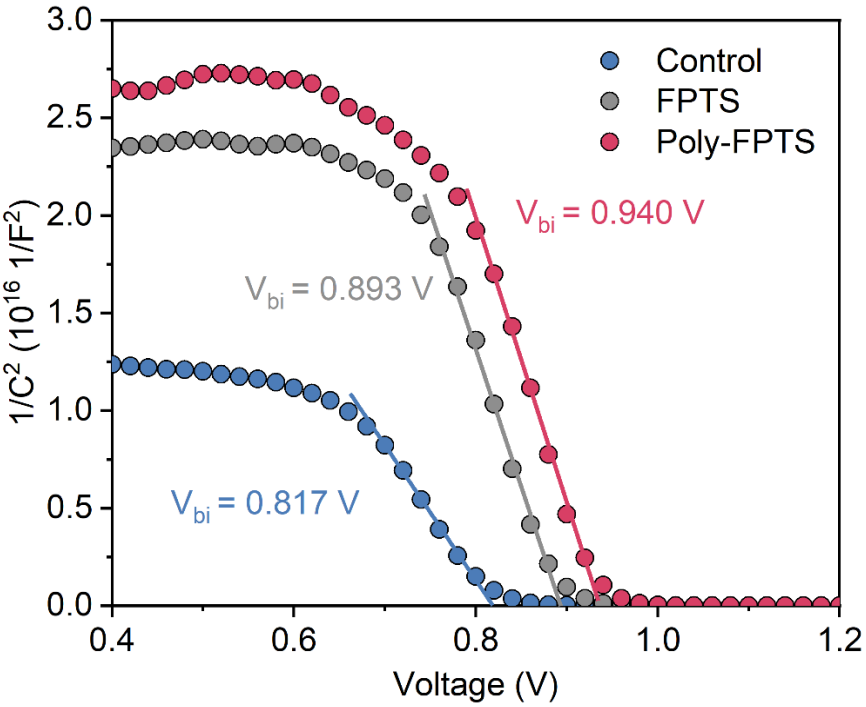

Figure S13. Mott-Schottky (M-S) measurements of untreated, FPTS-treated, and poly-FPTS-treated devices.

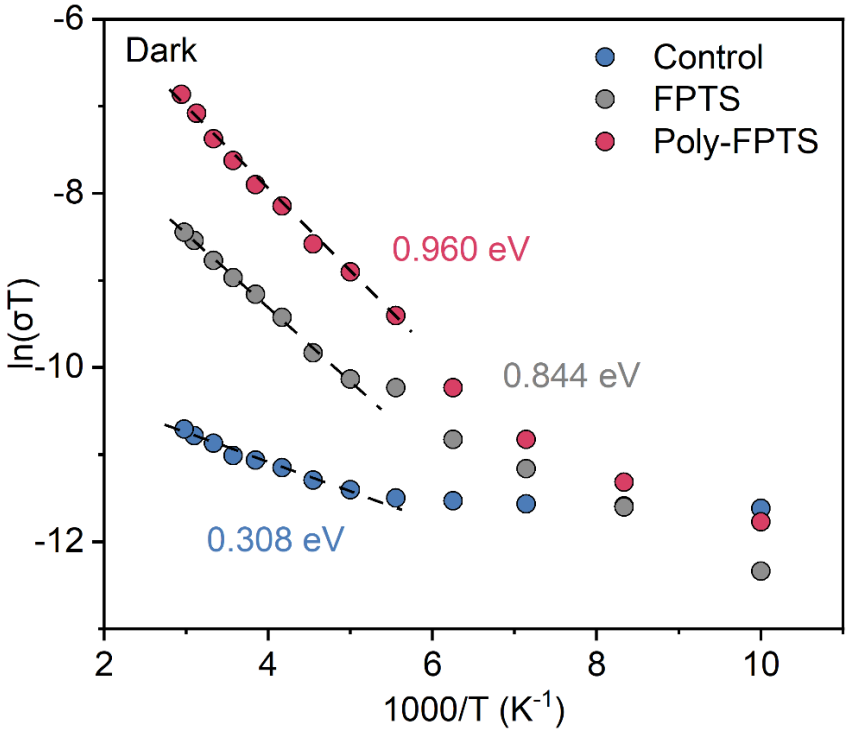

Figure S14. The ion migration activation energy (E_a) of the untreated, FPTS-treated, and poly-FPTS-treated perovskite devices under dark conditions.

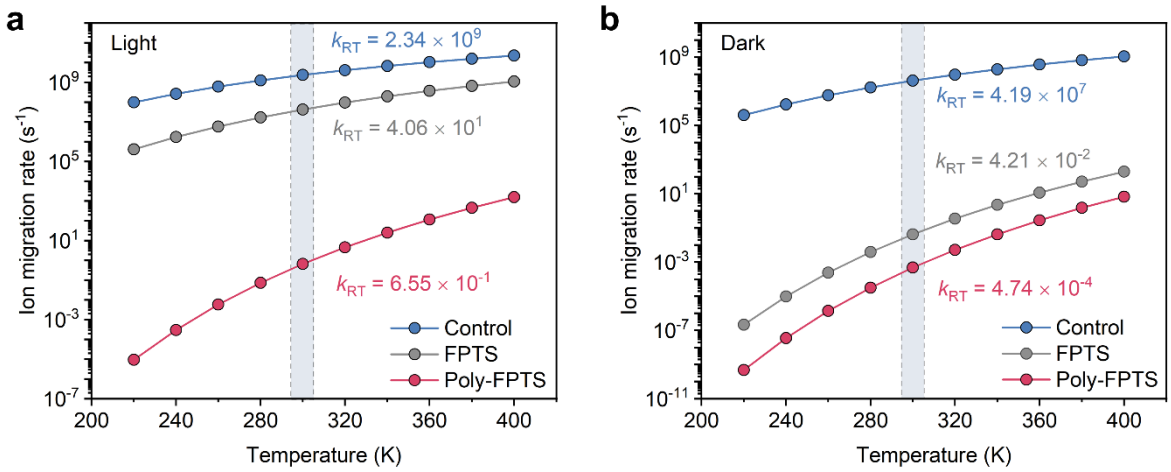

Figure S15. Calculated ion migration rates (k) of untreated, FPTS-treated, and poly-FPTS-treated perovskite devices under light (**a**) and dark (**b**) conditions.

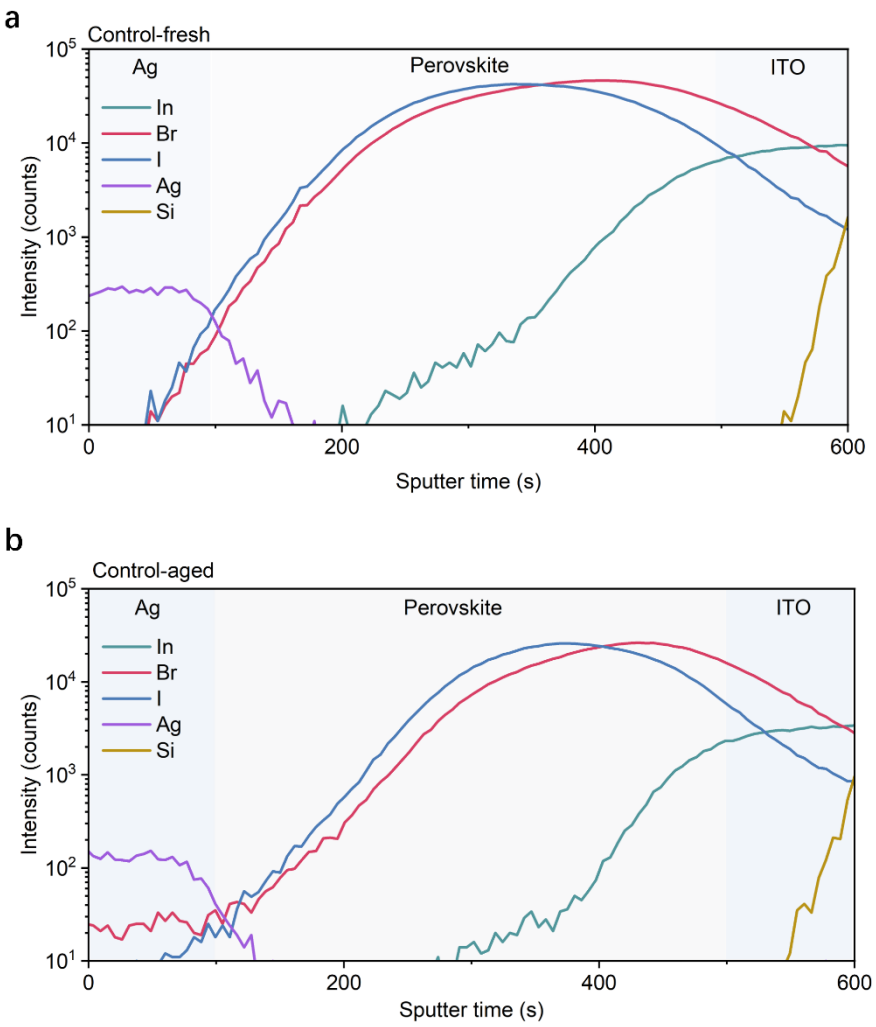

Figure S16. ToF-SIMS of untreated devices before (**a**) and after (**b**) illumination aging. The devices were aged 200 hours in a N_2-filled chamber under simulated one sun illumination using a white-light-emitting diode (LED).

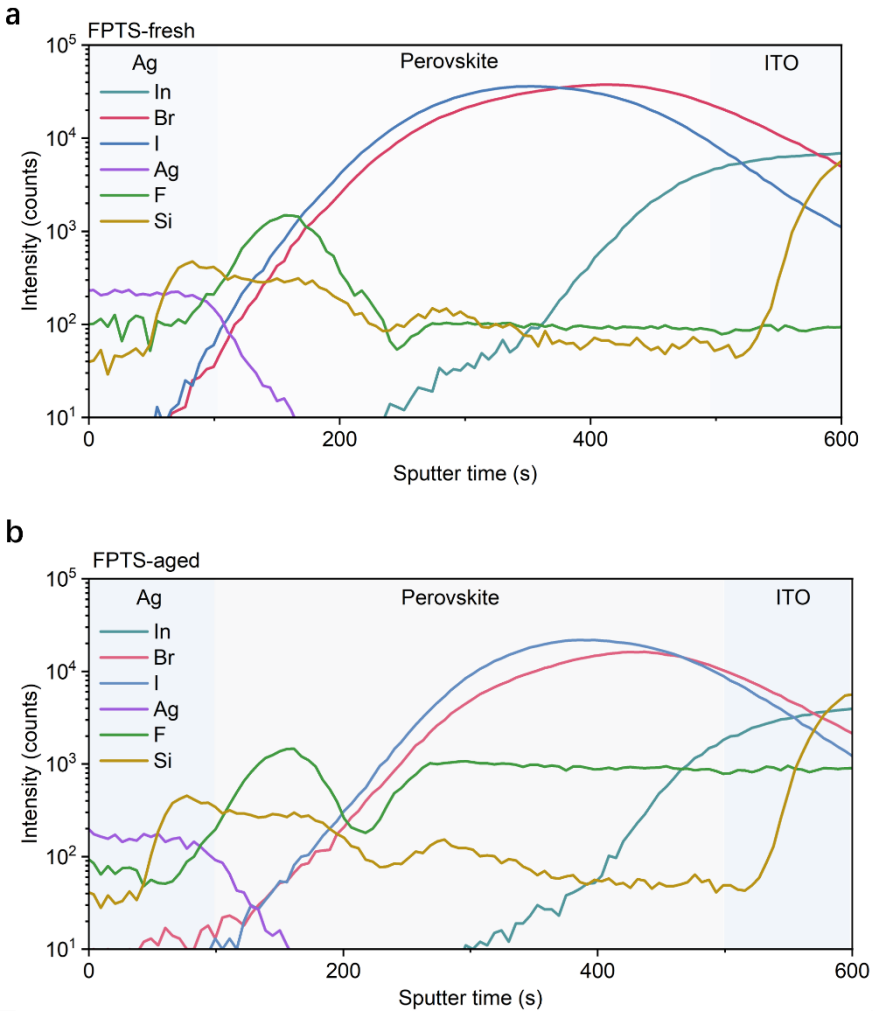

Figure S17. ToF-SIMS of FPTS-treated devices before (**a**) and after (**b**) illumination aging. The devices were aged for 200 hours in a N_2-filled chamber under simulated one sun illumination using a white-light-emitting diode (LED).

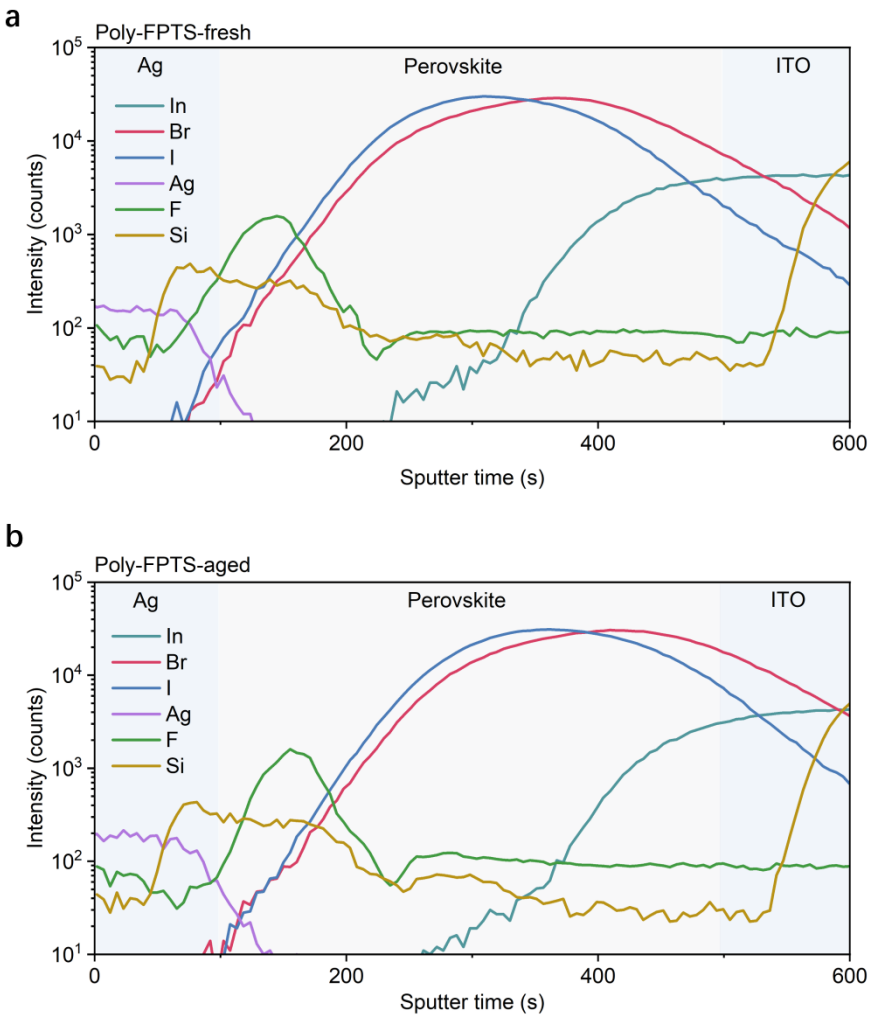

Figure S18. ToF-SIMS of poly-FPTS-treated devices before (**a**) and after (**b**) illumination aging. The devices were aged for 200 hours in a N_2-filled chamber under simulated one sun illumination using a white-light-emitting diode (LED).

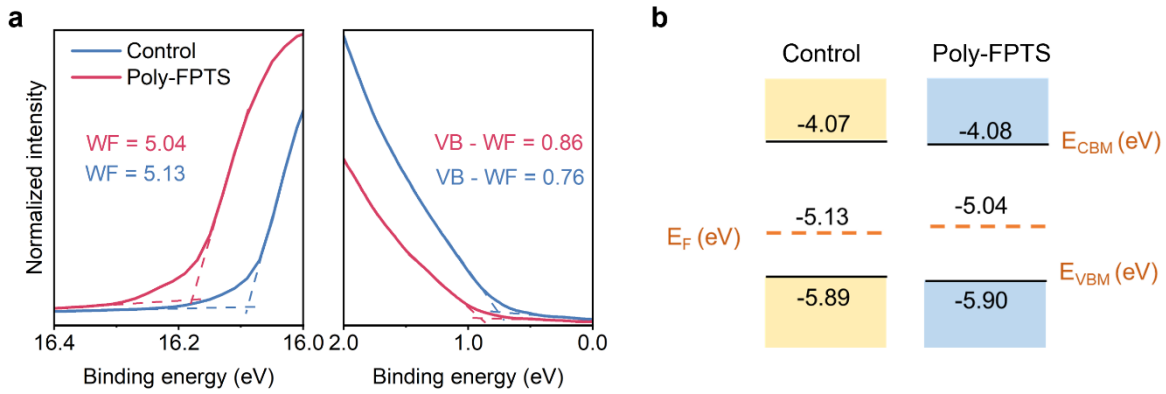

Figure S19. (**a**) UPS spectra of perovskite films without and with poly-FPTS treatment. (**b**) Energy level diagram of perovskite without and with poly-FPTS treatment.

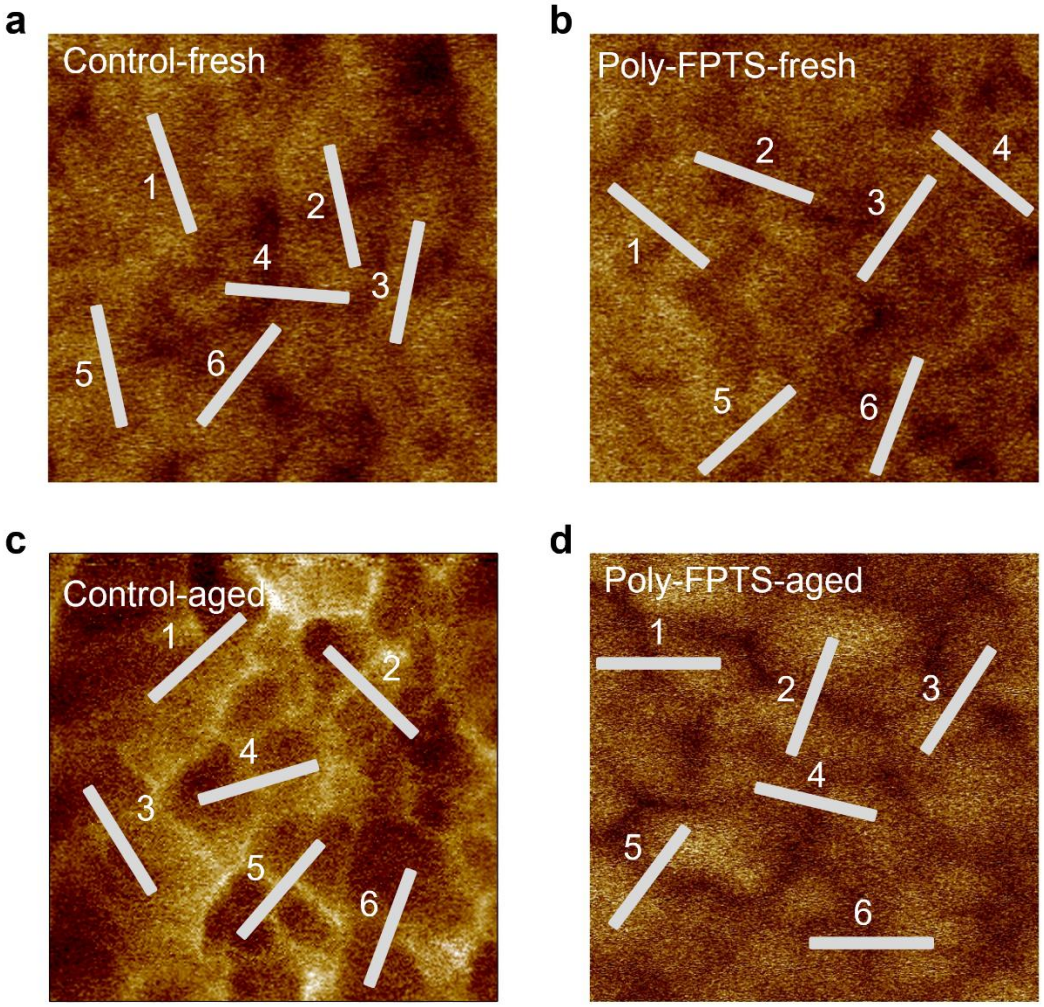

Figure S20. Surface contact potential for untreated (**a**) and poly-FPTS-treated (**b**) perovskite films before aging. Ex-situ surface contact potential for untreated (**c**) and poly-FPTS-treated (**d**) perovskite films after aging. The grey bar represents the collected line profiles across the grain boundaries in **Fig. 2a and 2b**.

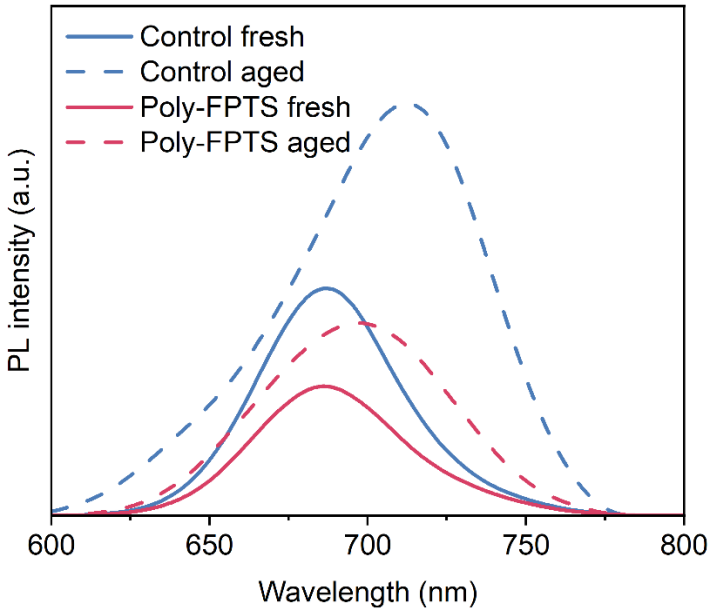

Figure S21. Steady-state PL spectrum of fresh and aged perovskite/ETL films without and with poly-FPTS treatment. The incident excitation light entered from the ETL side. The devices were aged under illumination for 24 hours.

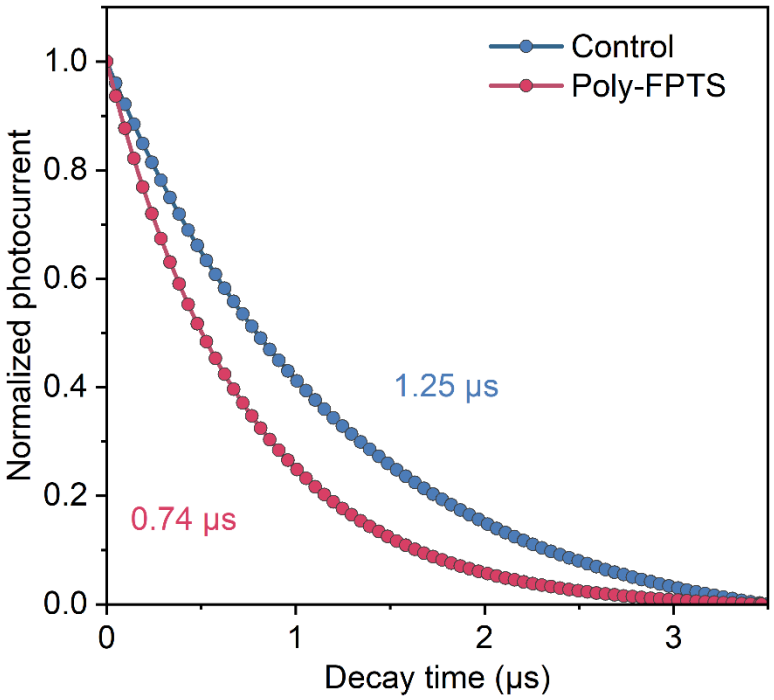

Figure S22. Transient photocurrent (TPC) decays of untreated and poly-FPTS-treated PSCs. See **Note S4** for fitting details.

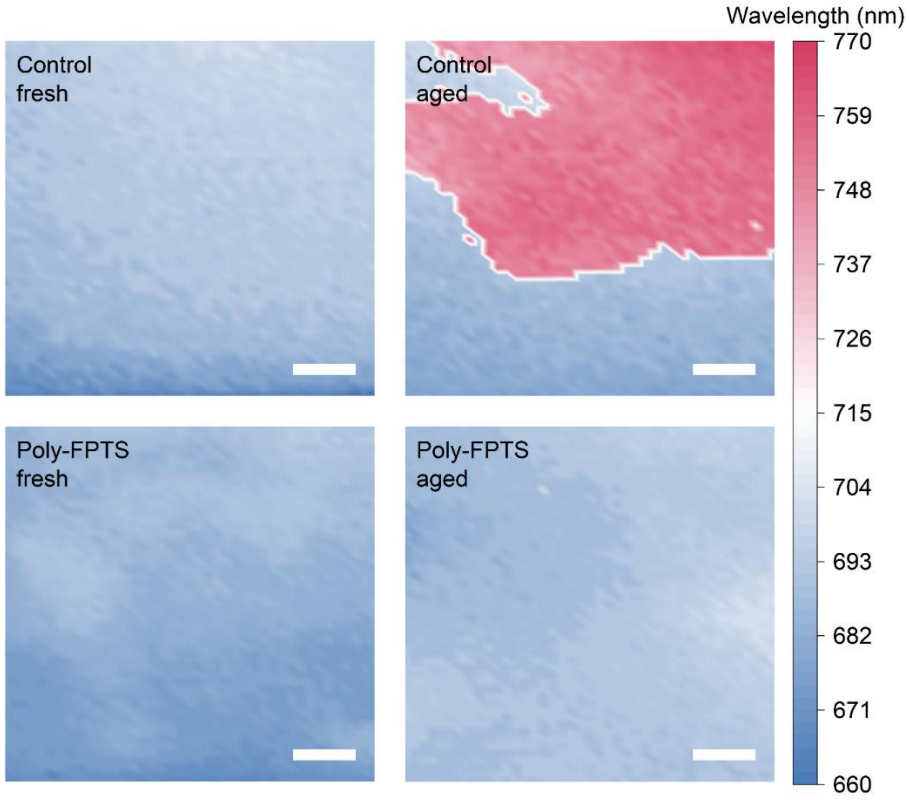

Figure S23. Ex-situ PL mapping for untreated and poly-FPTS-treated perovskite films before and after aging. The scale bar is 1μm.

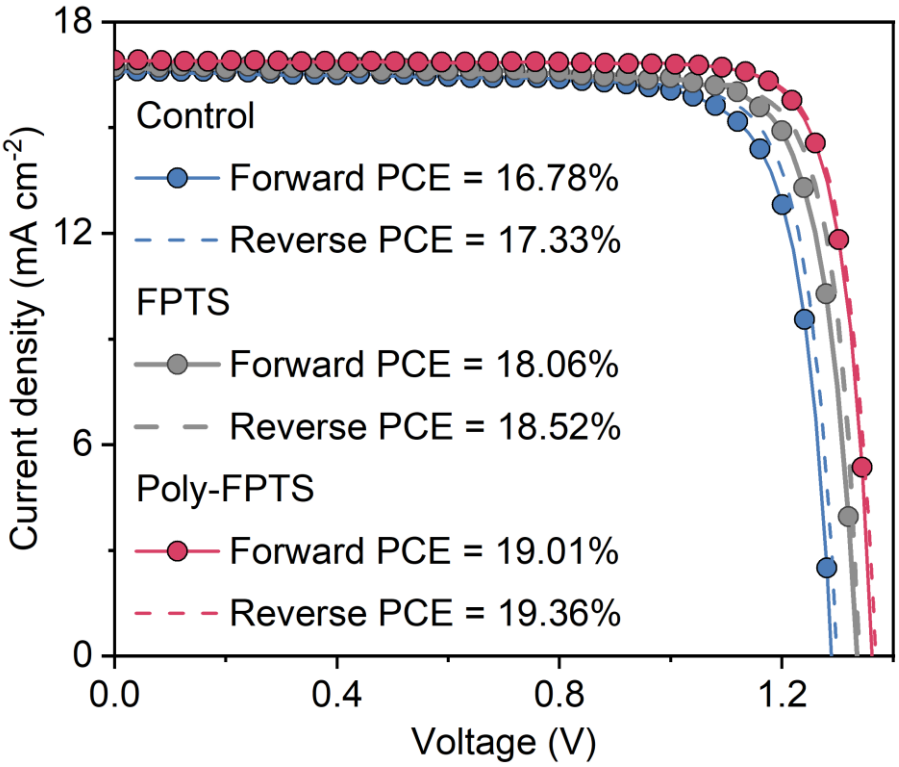

Figure S24. *J-V* curves of champion untreated and poly-FPTS-treated perovskite solar cells.

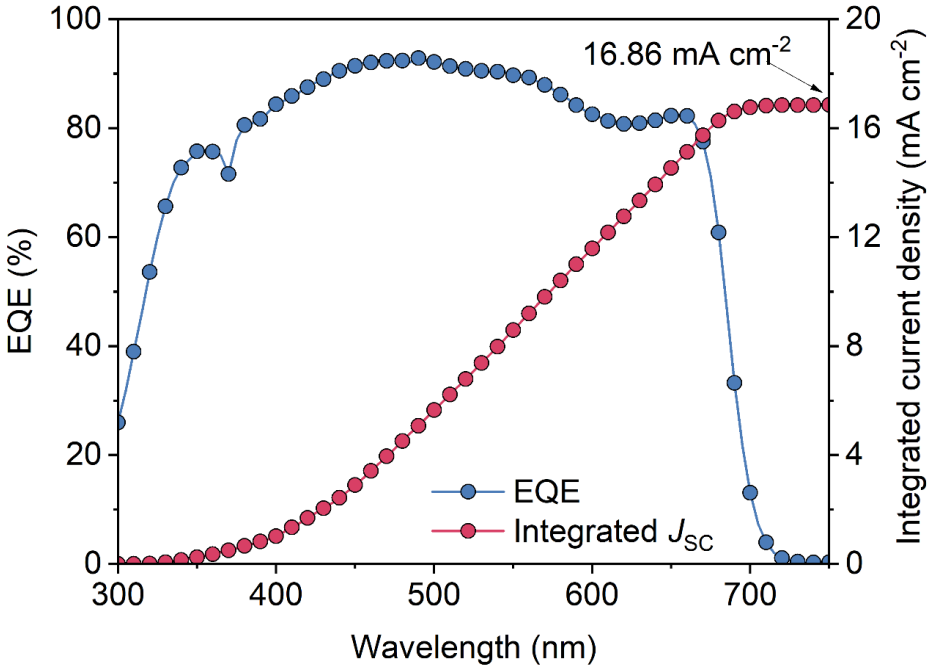

Figure S25. External quantum efficiency (EQE) curve with an integrated current density of 16.86 mA cm^{-2} for the poly-FPTS-treated PSC.

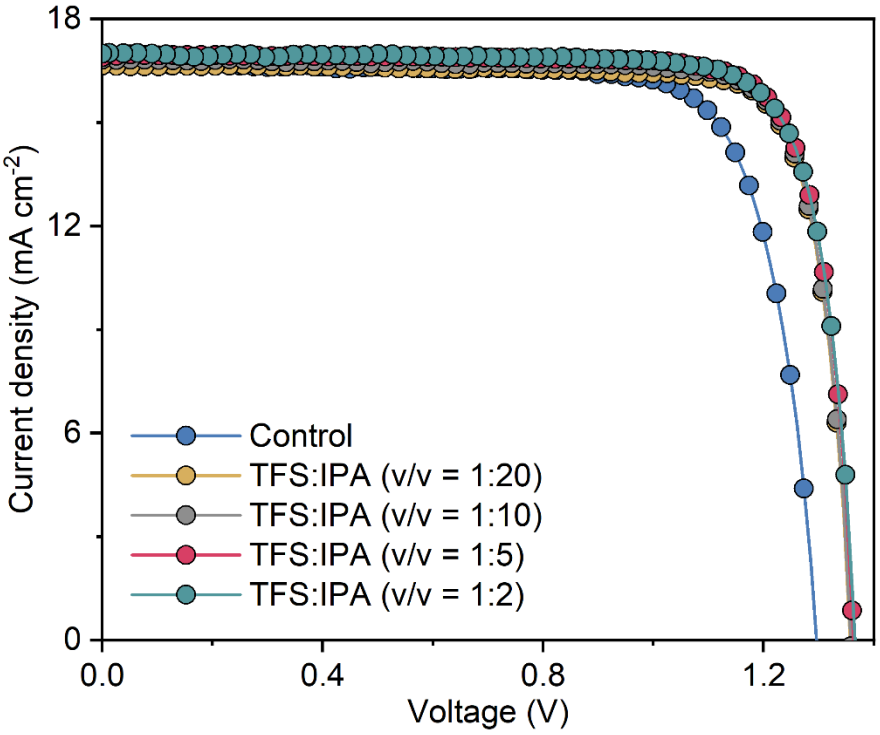

Figure S26. *J-V* curves of perovskite treated with different concentrations of poly-FPTS.

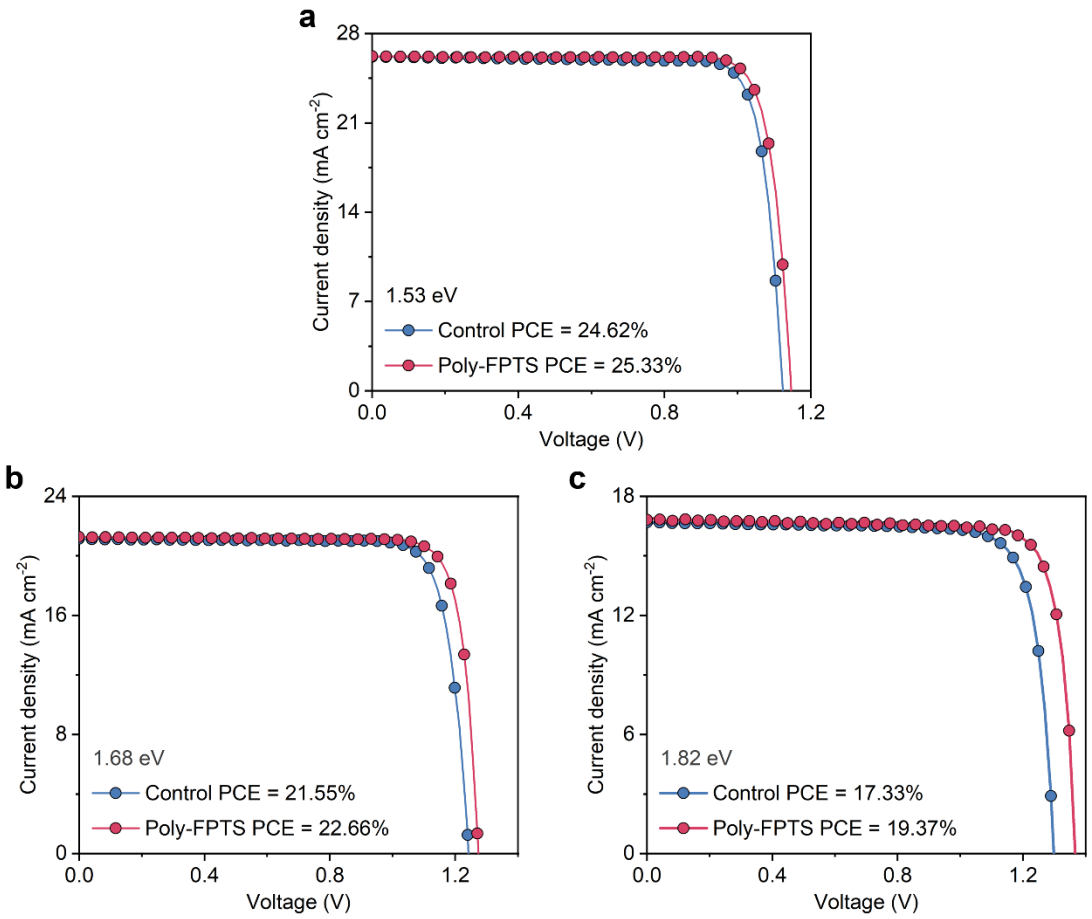

Figure S27. *J-V* curves of 1.53 eV (**a**), 1.68 eV (**b**) and 1.82 eV (**c**) perovskite solar cells without and with poly-FPTS treated.

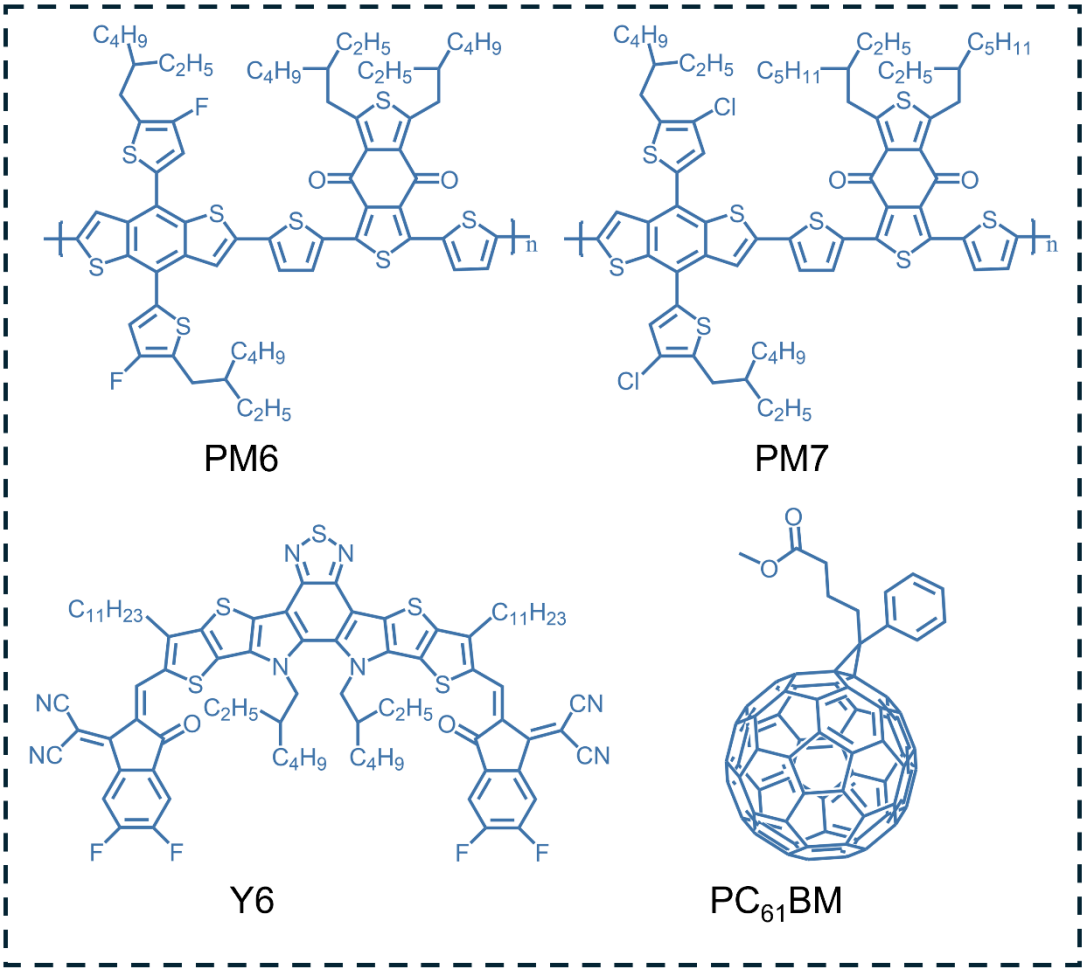

Figure S28. Chemical structures of PM6, PM7, Y6, and $PC_{61}BM$ were used in the organic photovoltaic layer.

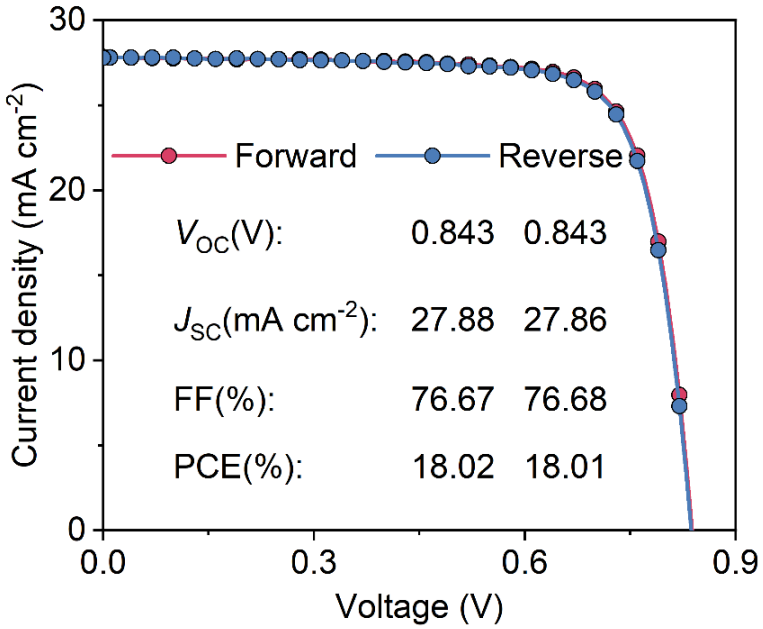

Figure S29. *J-V* curves parameters of organic single-junction devices under forward and reverse scan.

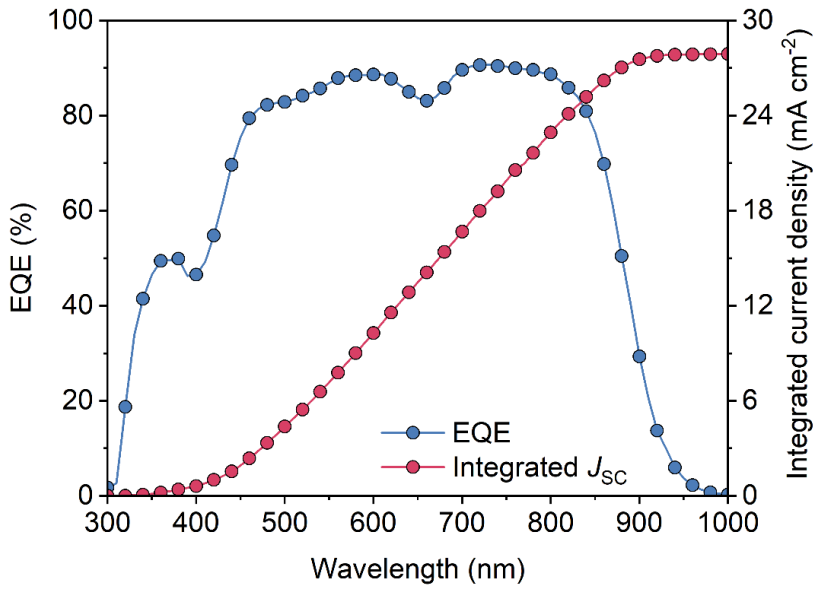

Figure S30. EQE curve with an integrated current density of 27.88 mA cm^{-2} for the OSCs.

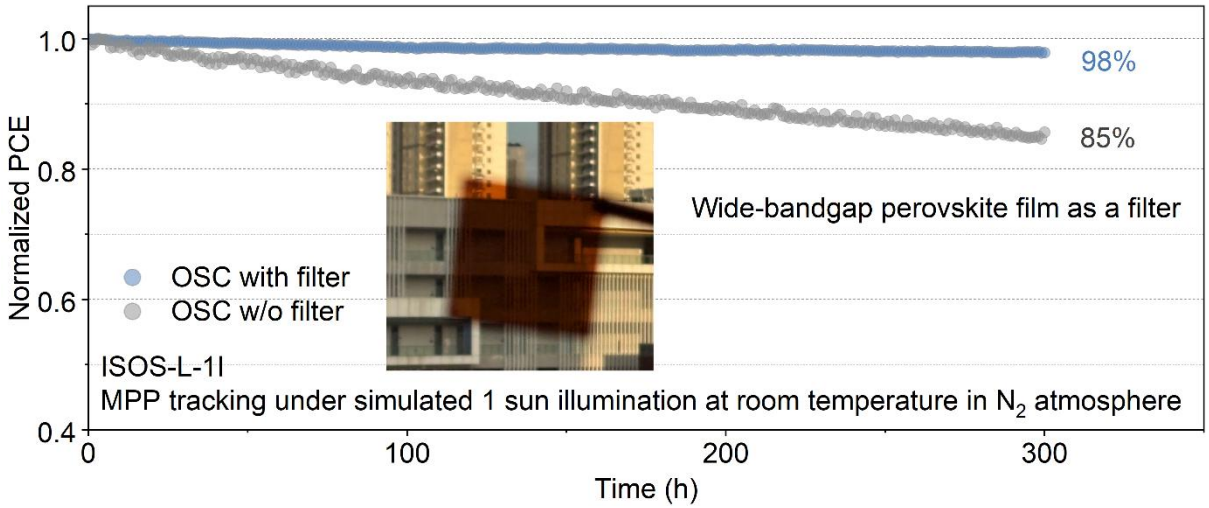

Figure. S31. Continuous MPP tracking of organic heterojunction solar cells for illumination in N_2 atmosphere without and with wide-bandgap perovskite films as a filter.

Note: Under full-spectrum illumination, the OSC retained approximately 85% of its initial efficiency after 300 hours. Crucially, under filtered spectral conditions (simulating tandem conditions), the organic solar cell (OSC) exhibited significantly enhanced stability, retaining approximately 98% of its initial performance after 300 hours of maximum power point tracking (MPPT).

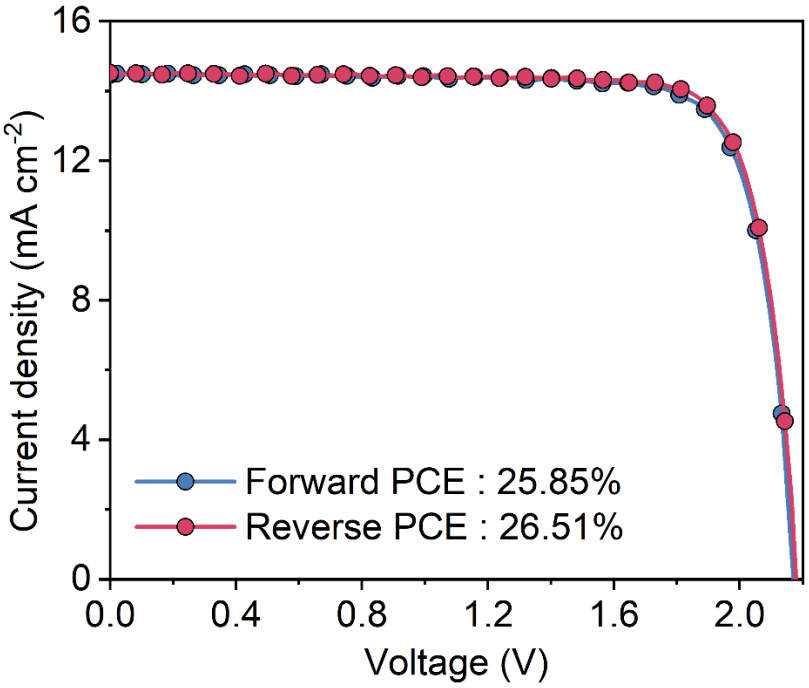

Figure S32. *J-V* curves of the champion POTSC under forward and reverse scans.

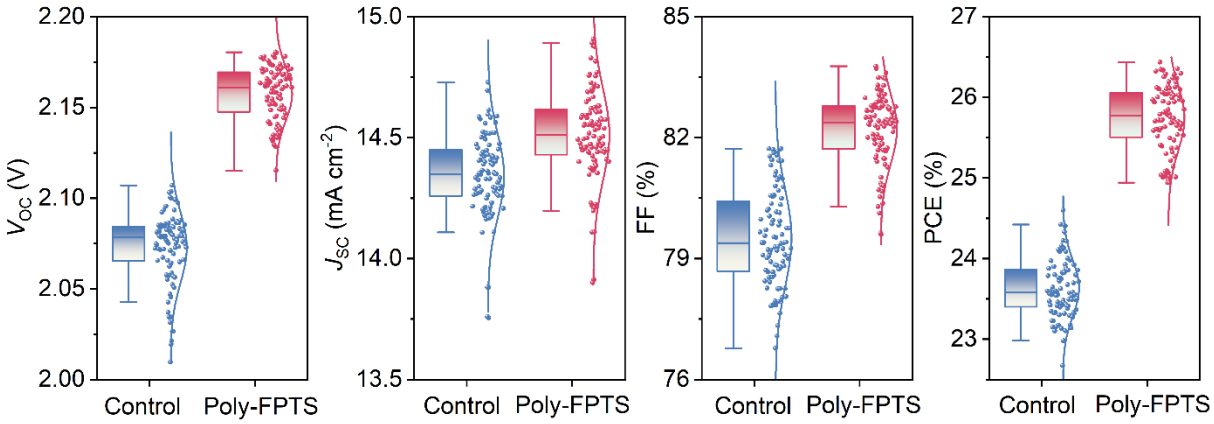

Figure S33. Device statistics are presented in box-and-whisker plots (center line: average, box limit: standard deviation, whiskers: outliers) for V_{OC}, J_{SC}, and FF and PCE for untreated and poly-FPTS-treated devices.

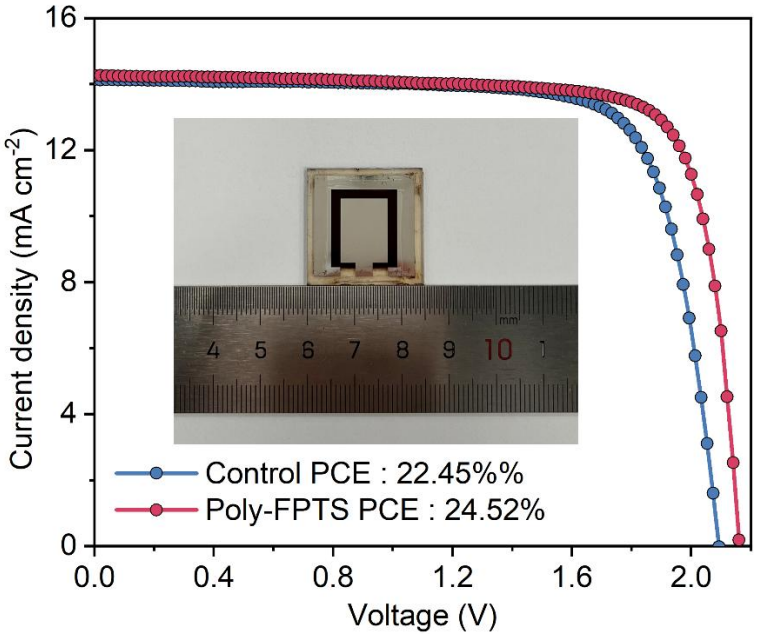

Figure S34. *J-V* curves of 1.05-cm^2 POTSCs without and with poly-FPTS treated.

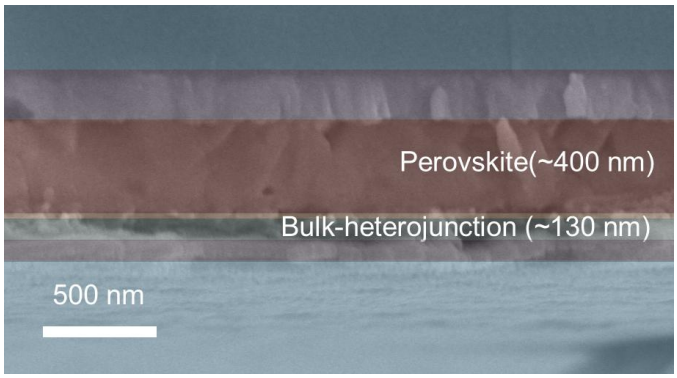

Figure S35. Cross-section SEM of POTSC devices. The scale bar is 500 nm.

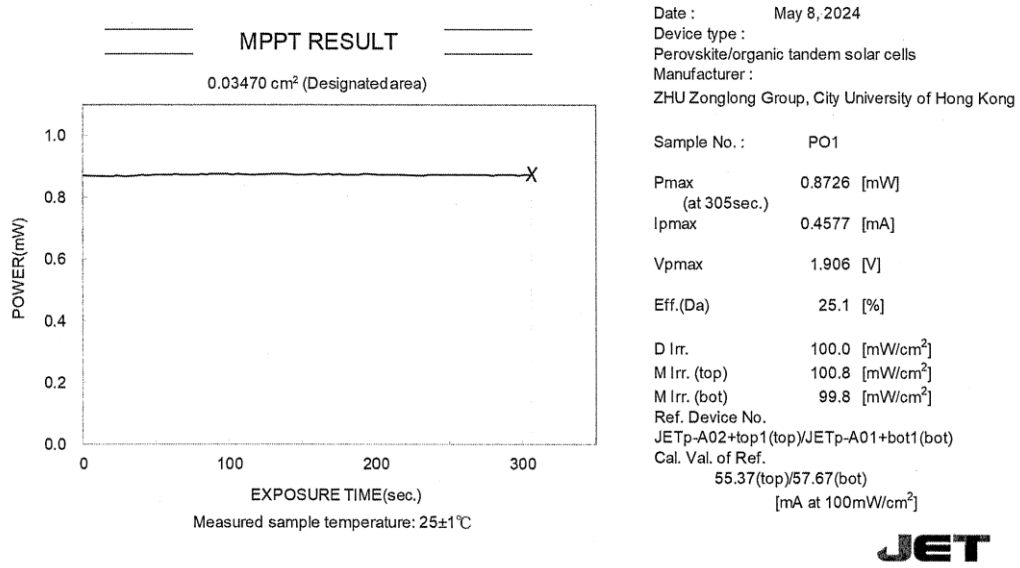

Figure S36. Certified results of POTSC with a steady-state PCE of 25.1%. Obtained copyright permission for use.

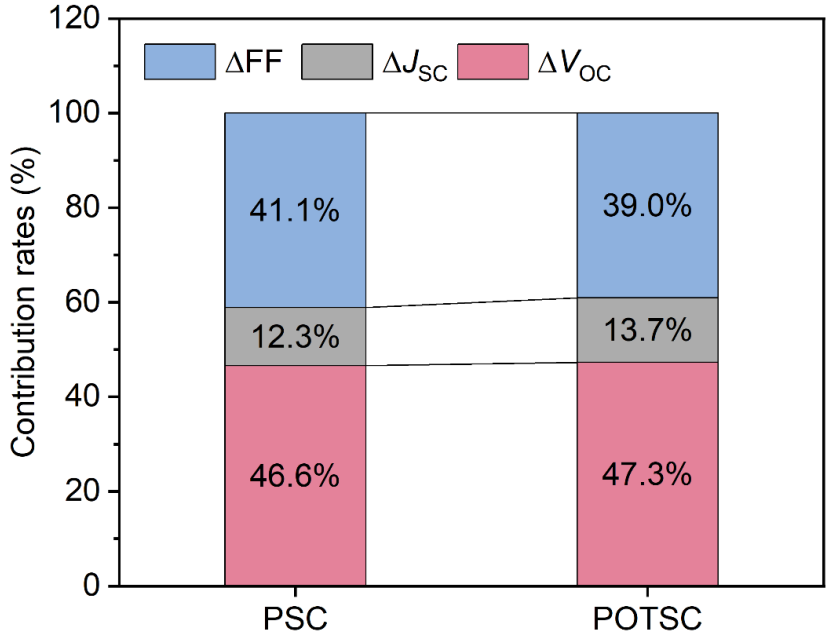

Figure S37. Contribution rates of photovoltaic parameters to the performance improvement of poly-FPTS-treated PSCs and POTSCs.

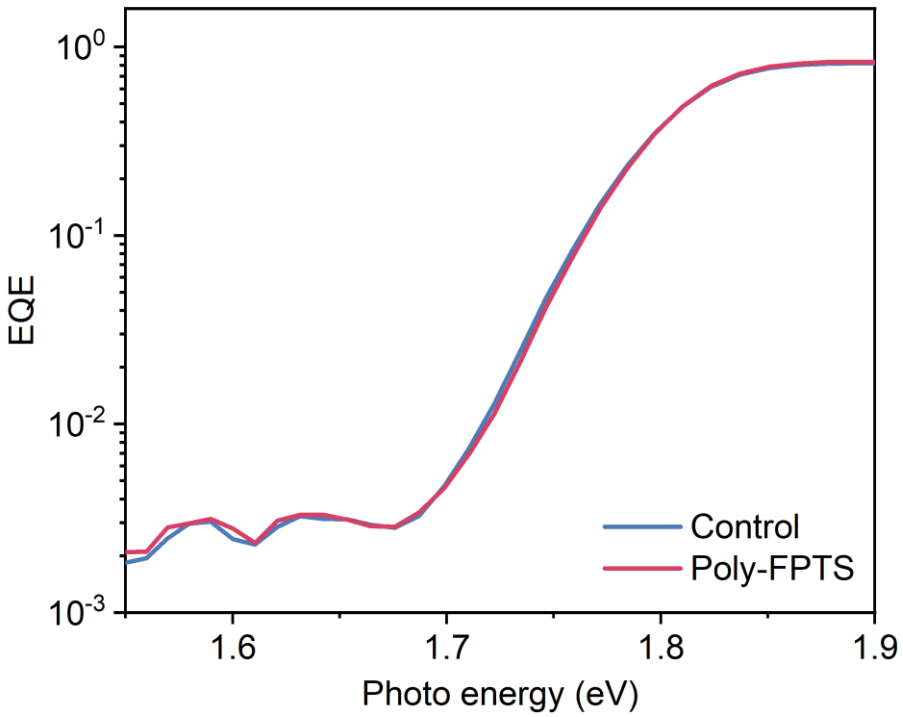

Figure S38. Highly sensitive EQE for perovskite devices without and with poly-FPTS treatment.

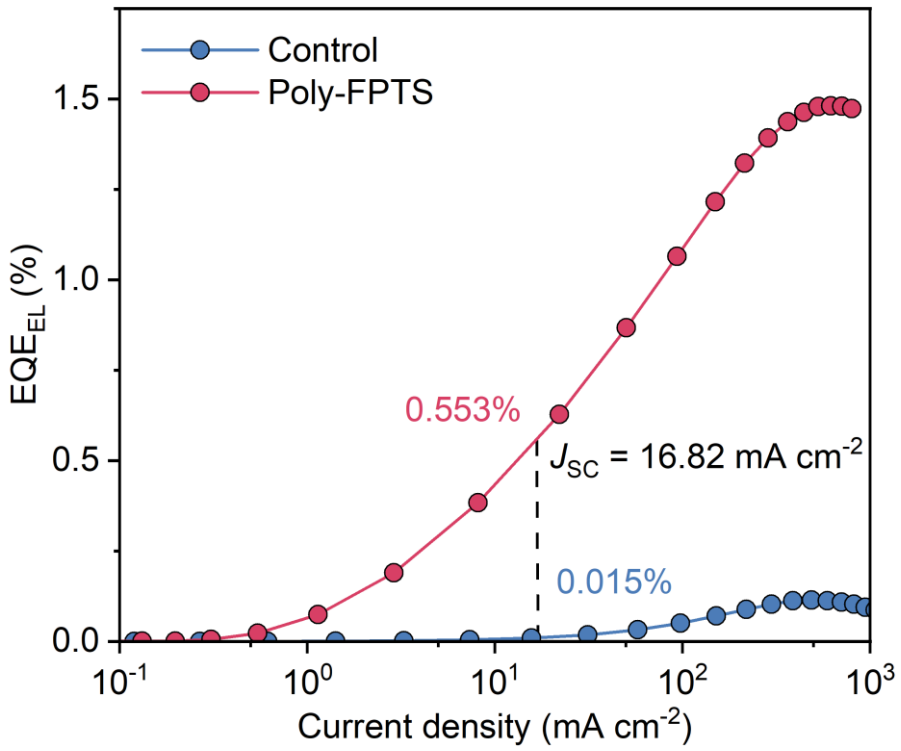

Figure S39. EQE_{EL} for perovskite devices without and with poly-FPTS treatment.

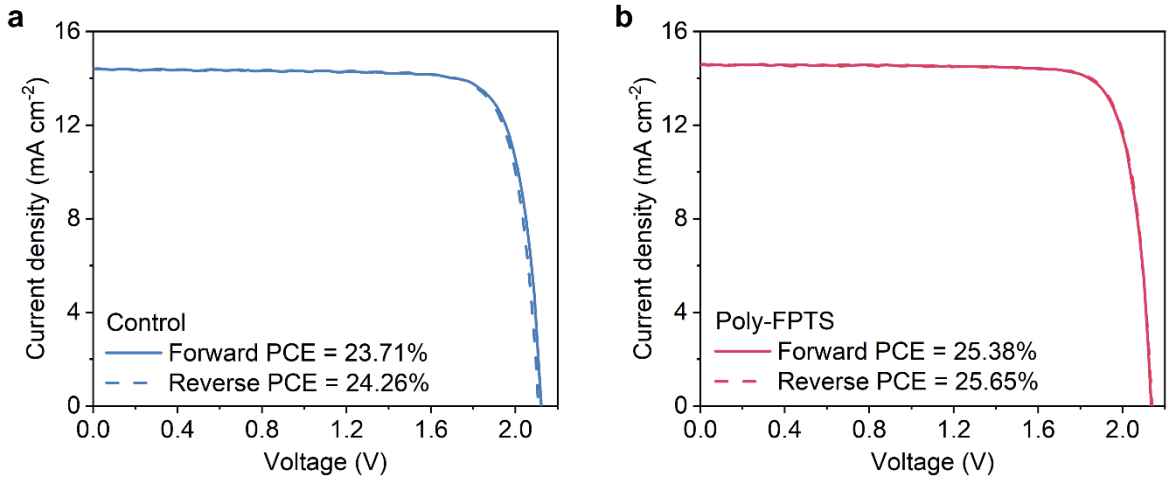

Figure S40. Initial *J-V* curves of encapsulated POTSCs without and with poly-FPTS treatment before thermal accelerated aging measurements.

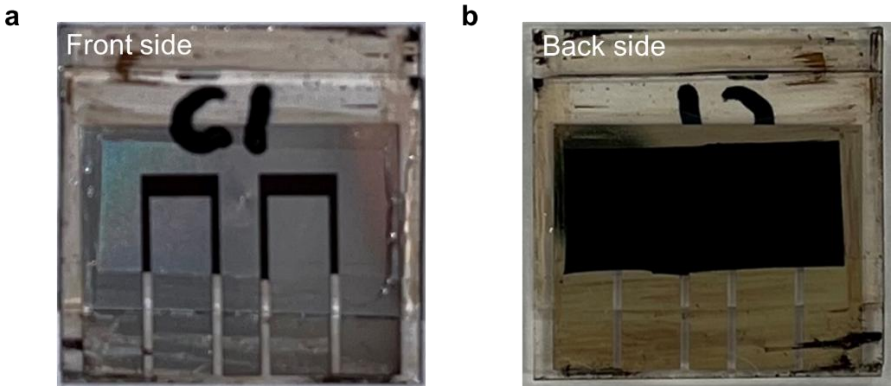

Figure S41. Representative photographs of the encapsulated device for operational stability.

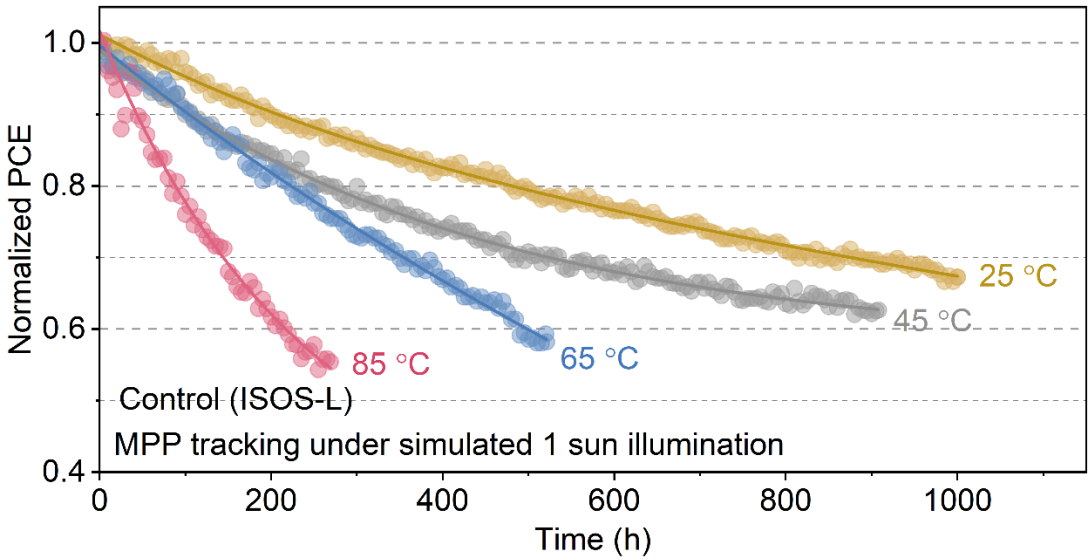

Figure S42. Operational stability of untreated POTSCs operating at 25℃, 45℃, 65℃, 85℃ (ISOS-L). The encapsulated devices were held at their MPP under simulated 1 sun illumination. The solid lines are a bi-exponential fit to the data.

Note S1. Bias-assisted charge extraction (BACE)

In dark BACE, the device was initially held at a voltage close to the open-circuit voltage (V_{pre}) where the injected charge equals the short-circuit current. After a pre-set delay time, a bias V_{coll} = 0V (or a reverse bias) was applied to extract the injected and capacitive charge in the device. To obtain the capacitive charge, the measurement was repeated from 0V to -V_{pre}. V_{pre} and V_{coll} were set by an Agilent 81150A pulse generator, allowing a fast extraction time of 150 ns. The current transients were measured via a 50 Ω resistor and recorded with an oscilloscope (Agilent DSO9104H). The extracted charge was obtained by integrating the current transient.

Note S2. Space charge limited current (SCLC) measurements

The electron-only and hole-only devices were fabricated for SCLC measurements to calculate the trap densities (N).[10] In the SCLC region, the current is primarily dominated by charge carriers injected from the contacts, and the current density-voltage characteristic exhibits a quadratic relationship (J~V^2). Measurement results are displayed on a double logarithmic coordinate system for the J-V curves of the fabricated devices, encompassing the ohmic region ($J \propto V$), the trap-filling-limited (TFL) region ($J \propto V^n, n > 2$), and the child region ($J \propto V^2$). In the TFL region, the trap state density (N_t) can be calculated by the following equation:

$$N_t = \frac{2\varepsilon\varepsilon_0 V_{\text{ons}}}{qL^2}$$

where $\varepsilon = 26$ and $\varepsilon_0 = 8.85\text{e-}12$ F m^{-1} are the relative dielectric constant and vacuum permittivity, respectively. V_{ons} is the onset voltage of TFL region, q is elementary charge. L represents thickness of perovskite thin film (400 nm).

Note S3. Ion migration rate

Temperature-dependent conductivity measurements for deriving ion migration Ea were conducted using an N_2 cryostat (Optistat DN-V, Oxford Instruments). The temperature was controlled by a cryogenic environment controller (Mercury iTC, Oxford Instruments). The device is first cooled and stabilized at 100K for 30 min. Then the device is slowly heated to 340 K with a step of 20 K. All temperatures were stabilized for 15 min before measurement. A Keithley 2400 was used to apply a voltage bias and measure the current. The E_a is obtained through the Nernst-Einstein relation:

$$\sigma T = \sigma_0 \exp\left(-\frac{E_a}{k_B T}\right)$$

where σ_0 is a constant, k_B is Boltzmann's constant, σ is ionic conductivity, T is temperature, and E_a is the ion-migration activation energy. We derived E_a values from the ln(σT) slope versus 1/T. Given the E_a, we can estimate that the ion migration rates (k) at the corresponding temperature based on the Arrhenius equation:

$$k = (k_B T)/\hbar \exp\left(-\frac{E_a}{RT}\right)$$

where k_B stands for the Boltzmann constant, T is the temperature, $\hbar$ is the reduced Planck constant, and R is the ideal gas constant.[11,12]

Note S4. TPC characterizations

This study employs transient photocurrent (TPC) technology to characterize the charge-transport performance of devices near the maximum power point (i.e., under short-circuit conditions). This method directly reflects the dynamics of charge extraction at the electrodes by measuring the transient current decay induced by a small optical perturbation. Under a strong extraction field, in an idealized state where the carrier transport path is relatively uniform and the trapped state effect is not dominant, the current decay can be approximated by a single exponential function:[13]

$$I(\tau) = Aexp\left(-\frac{\tau}{\tau_{tpc}}\right) + C$$

Where *A is* the initial amplitude, τ_{tpc} is the charge transport time constant, and *C* is the constant offset. τ_{tpc} can be obtained by fitting using a nonlinear least squares method.

For the device studied in this work, the charge transport process is mainly dominated by a single characteristic timescale. Therefore, τ_{tpc}, extracted using single exponential fitting, can serve as a robust and physically meaningful core parameter for comparing the relative transport performance differences between different devices.

Note S5. Calculation of V_{OC} Loss

The detailed $V_{OC,\,loss}$ analysis can be described by the equation listed below:[14]

$$q\Delta V = E_g - qV_{OC}$$

$$= \left(E_g - qV_{OC}^{SQ}\right) + \left(qV_{OC}^{SQ} - qV_{OC}^{rad}\right) + \left(qV_{OC}^{rad} - qV_{OC}\right)$$

$$= \left(E_g - qV_{OC}^{SQ} + q\Delta V_{OC}^{SQ}\right) + q\Delta V_{OC}^{rad} + q\Delta V_{OC}^{non-rad}$$

where q, ΔV, E_g is the elementary charge, the total voltage loss, and the bandgap of perovskite, respectively. V_{OC}^{SQ} is the S-Q limit of open circuit voltage, V_{OC}^{rad} is the V_{OC} without non-radiative recombination occurring in PSCs, ΔV_{OC}^{SQ} is the V_{OC} loss due to the non-ideal EQE above the bandgap, ΔV_{OC}^{rad} is the V_{OC} loss due to the sub-bandgap radiative recombination, and $\Delta V_{OC}^{non-rad}$ is the V_{OC} loss of non-radiative recombination. The calculation method was following detailed balance theory. Therefore, the energy loss can be divided into three parts, ΔV_1, ΔV_2 and ΔV_3, which represent radiative recombination above E_g, energy loss from blackbody radiation and voltage loss induced by the nonradiative recombination, respectively. According to the reciprocity relationship between photovoltaic external quantum efficiency ($\mathrm{EQE_{PV}}$) and electroluminescence (EL), the V_{OC} of a solar cell can be calculated with the equation listed below:

$$V_{\mathrm{OC}} = \frac{k_{\mathrm{B}}T}{q}\ln\left(\frac{J_{\mathrm{SC}}}{J_0}\right)$$

where q is element charge, k_{B} is Boltzmann constant, T is temperature, J_{SC} is short-circuit current, J_0 is dark saturation current. The expressions of J_{SC} and J_0 are given by:

$$J_{\mathrm{SC}} = q\int_0^{\infty} \mathrm{EQE_{PV}}(E)\phi_{\mathrm{AM1.5}}(E)\,dE$$

$$J_0 = \frac{q}{\mathrm{EQE_{EL}}}\int_0^{\infty} \mathrm{EQE_{PV}}(E)\phi_{\mathrm{BB}}(E)\,dE$$

$$\phi_{\mathrm{BB}}(E) = \frac{2\pi E^2}{h^3c^2}\frac{1}{\exp\left(\frac{E}{k_{\mathrm{B}}T}\right) - 1}$$

where $\mathrm{EQE_{EL}}$ is EL external quantum efficiency, $\phi_{\mathrm{AM1.5}}$ is solar cell radiative spectrum, ϕ_{BB} is black-body radiative spectrum, c is light speed in vacuum.

In Shockley-Queisser limit (S-Q limit): (1) The $\mathrm{EQE_{PV}}$ is described with Heaviside step

function, where $\mathrm{EQE_{PV}}(E) = \begin{cases} 1, E \geq E_\mathrm{g} \\ 0, E < E_\mathrm{g} \end{cases}$; (2) only the photos with energy larger than bandgap (E_g) are absorbed; (3) all recombination is radiative ($\mathrm{EQE_{EL}} = 1$). Therefore, J_SC and J_0 in S-Q limit are written as:

$$J_\mathrm{SC}^\mathrm{SQ} = q \int_{E_\mathrm{g}}^{\infty} \phi_\mathrm{AM1.5}(E)\, dE$$

$$J_0^\mathrm{SQ} = q \int_{E_\mathrm{g}}^{\infty} \phi_\mathrm{BB}(E)\, dE$$

Therefore, V_OC in S-Q limit is:

$$V_\mathrm{OC}^\mathrm{SQ} = \frac{k_\mathrm{B}T}{q} \ln\left(\frac{J_\mathrm{SC}^\mathrm{SQ}}{J_0^\mathrm{SQ}}\right)$$

Considering the assumption of S-Q limit, $V_\mathrm{OC}^\mathrm{SQ}$ can be degraded to V_OC with 3 loss components. The first V_OC loss component, $\Delta V_\mathrm{OC}^\mathrm{SQ}$, is due to the non-ideal $\mathrm{EQE_{PV}}$, which is less than 100%. In this condition, short-circuit current is expressed as:

$$J_\mathrm{SC} = q \int_{0}^{\infty} \mathrm{EQE_{PV}}(E) \phi_\mathrm{AM1.5}(E)\, dE$$

$\Delta V_\mathrm{OC}^\mathrm{SQ}$ is calculated as:

$$\Delta V_\mathrm{OC}^\mathrm{SQ} = V_\mathrm{OC}^\mathrm{SQ} - \frac{k_\mathrm{B}T}{q} \ln\left(\frac{J_\mathrm{SC}}{J_0^\mathrm{SQ}}\right) = \frac{k_\mathrm{B}T}{q} \ln\left(\frac{J_\mathrm{SC}^\mathrm{SQ}}{J_\mathrm{SC}}\right)$$

The second V_OC loss component arises from the energy loss associated with the extra thermal radiation emitted by the solar cell in the dark. In the experiment, the $\mathrm{EQE_{PV}}$ extends into the sub-bandgap region, where the black-body radiation increases with the photo energy lowering. Thus, this sub-bandgap $\mathrm{EQE_{PV}}$ increased the dark saturation current. The dark saturation current in this condition is written as:

$$J_0^\mathrm{rad} = q \int_{0}^{\infty} \mathrm{EQE_{PV}}(E) \phi_\mathrm{BB}(E)\, dE$$

Therefore, the radiative V_OC loss, $\Delta V_\mathrm{OC}^\mathrm{rad}$, is:

$$\Delta V_\mathrm{OC}^\mathrm{rad} = \frac{k_\mathrm{B}T}{q} \ln\left(\frac{J_\mathrm{SC}}{J_0^\mathrm{SQ}}\right) - \frac{k_\mathrm{B}T}{q} \ln\left(\frac{J_\mathrm{SC}}{J_0^\mathrm{rad}}\right) = \frac{k_\mathrm{B}T}{q} \ln\left(\frac{J_0^\mathrm{rad}}{J_0^\mathrm{SQ}}\right)$$

The third V_{OC} loss component, ΔV_{OC}^{nonrad}, is ascribed to the non-radiative recombination in device, which can be calculated as:

$$\Delta V_{OC}^{nonrad} = \frac{k_B T}{q} \ln\left(\frac{J_{SC}}{J_0^{rad}}\right) - V_{OC}$$

According to previous equations and $J_0^{rad} = EQE_{EL} \cdot J_0$, the equation above can be rewritten as:

$$\Delta V_{OC}^{nonrad} = \frac{k_B T}{q} \ln\left(\frac{J_{SC}}{EQE_{EL} \cdot J_0}\right) - \frac{k_B T}{q} \ln\left(\frac{J_{SC}}{J_0}\right) = -\frac{k_B T}{q} \ln(EQE_{EL})$$

Note S6. Accelerated aging test of perovskite-based tandem solar cells operating at different temperatures.

The temperature dependence of the PCE degradation rate can be fitted to a biexponential function, according to Loo et al.'s work.[15]

$$PCE\ (t) = A1 \times \exp\left(-k_{fast} \times t\right) + A2 \times \exp(-k_{slow} \times t) + B$$

where $A1$, $A2$, and B are constant, t represents time. A fast and slow degradation rate (k_{fast} and k_{slow}) can be extracted from the fitting results with an $R^2 > 0.95$, except for the data extracted from the control and poly-FPTS POTSCs operating at 25°C, since these devices showed less than 10% of efficiency loss within 1,000 hours. The comparable k_{fast} and k_{slow} of three types of devices indicated that the two degradation rates probed a single physical process, suggesting a reliable accelerated aging test.

The activation energies (E_a) related to degradation rates can be estimated from a single Arrhenius function across the entire temperature range.[16–18] We use the value of k_{slow} to obtain E_a in the following calculation, since k_{slow} is mainly responsible for the device's long-term degradation.

$$E_{\mathrm{a}} = -\frac{\partial \ln\left(k(T)\right)}{\partial\left(\frac{1}{k_B T}\right)}$$

where $k(T)$ is a degradation rate at temperature T, A is a constant, E_a is the activation energy of degradation, and k_B is Boltzmann's constant. The temperature-dependent slow degradation rate was plotted as a function of inverse temperature. A practical accelerated stress test can quantify the lifetime acceleration factor (AF), which relates to the lifetime under a defined standard operating condition (defined as 1-sun illumination at 25 °C), k_{ref}, under elevated stress conditions, k_{acc}.

$$AF = \frac{k_{\mathrm{acc}}}{k_{\mathrm{ref}}} = \exp\left[\frac{E_a}{k_B}\left(\frac{1}{T_{\mathrm{ref}}} - \frac{1}{T_{\mathrm{acc}}}\right)\right]$$

Supplementary tables

Table S1. TRPL fitted parameters. Transient absorption fitted kinetics parameters for perovskite films without and with surface treatment.

	A_1	τ_1	A_2	τ_2	τ_{ave} (ns)
Control (fresh)	1667.6	21.8	314.1	134.2	82.2
Poly-FPTS (fresh)	4763.1	13.3	119.8	104.1	28.2
Control (aged)	2858.2	21.9	307.0	234.8	135.8
Poly-FPTS (aged)	2482.1	23.6	389.8	112.2	61.5

The results are fitted with the following bi-exponential equation:[19]

$$y = y_0 + A_1 exp(-\frac{t}{\tau_1}) + A_2 exp(-\frac{t}{\tau_2})$$

The average decay time is calculated through the following format:

$$\tau_{ave} = \frac{A_1\tau_1^2 + A_2\tau_2^2}{A_1\tau_1 + A_2\tau_2}$$

where τ_{ave} is the average lifetime, the shorter lifetime τ_1 represents the decay time of trap-mediated recombination, the longer lifetime τ_2 represents the decay time of radiative recombination, and $A1$ and $A2$ are the amplitudes, respectively.

Table S2. Photovoltaic performance parameters of untreated and poly-FPTS-treated perovskite solar cells at forward and reverse scan, under the illumination of AM 1.5G, 100 mW cm^{-2}.

	V_{OC} (V)	J_{SC} (mA cm^{-2})	FF (%)	PCE (%)
Control forward	1.286	16.61	78.59	16.78
Control reverse	1.296	16.59	80.60	17.33
FPTS forward	1.333	16.73	80.99	18.06
FPTS reverse	1.333	16.72	83.09	18.52
Poly-FPTS forward	1.357	16.85	83.15	19.01
Poly-FPTS reverse	1.366	16.83	84.24	19.37

Table S3. Photovoltaic performance parameters of untreated and poly-FPTS-treated PSCs with different dilution ratios in IPA, under AM 1.5G, 100 mW cm^{-2}.

	V_{OC} (V)	J_{SC} (mA cm^{-2})	FF (%)	PCE (%)
untreated	1.295	16.6	79.01	16.98
1:20	1.357	16.55	84.05	18.87
1:10	1.358	16.74	83.50	18.98
1:5	1.363	16.82	84.26	19.32
1:2	1.365	16.91	83.13	19.19

Table S4. Photovoltaic performance parameters of untreated and poly-FPTS-treated PSCs with bandgap of 1.53 eV, 1.68 eV and 1.82 eV, under the illumination of AM 1.5G, 100 mW cm^{-2}.

PSC	Condition	V_{OC} (V)	J_{SC} (mA cm^{-2})	FF (%)	PCE (%)
1.53 eV	Control	1.121	26.17	83.92	24.62
	Poly-FPTS	1.145	26.22	84.38	25.33
1.68 eV	Control	1.239	21.12	82.35	21.55
	Poly-FPTS	1.274	21.26	83.67	22.66
1.82 eV	Control	1.296	16.59	80.61	17.33
	Poly-FPTS	1.366	16.83	84.24	19.37

Table S5. Photovoltaic performance parameters of OSCs at forward and reverse scan, under the illumination of AM 1.5G, 100 mW cm^{-2}.

	V_{OC} (V)	J_{SC} (mA cm^{-2})	FF (%)	PCE (%)
forward	0.843	27.88	76.67	18.02
reverse	0.843	27.86	76.68	18.01

Table S6. Photovoltaic performance parameters of the single-junction PSC, the single-junction OSC and the POTSC at reverse scan, under the illumination of AM 1.5G, 100 mW cm^{-2}.

	V_{OC} (V)	J_{SC} (mA cm^{-2})	FF (%)	PCE (%)
Perovskite subcell	1.368	16.83	84.15	19.37
Organic subcell	0.843	27.88	76.67	18.02
Tandem	2.178	14.52	83.32	26.51

Table S7. Photovoltaic performance parameters of untreated and poly-FPTS-treated POTSCs at forward and reverse scan, under the illumination of AM 1.5G, 100 mW cm^{-2}.

	V_{OC} (V)	J_{SC} (mA cm^{-2})	FF (%)	PCE (%)
Control forward	2.097	14.43	78.72	23.82
Control reverse	2.106	14.45	80.86	24.61
Poly-FPTS forward	2.169	14.49	82.24	25.85
Poly-FPTS reverse	2.178	14.52	83.83	26.51

Table S8. Photovoltaic performance parameters of untreated and poly-FPTS-treated POTSCs with different dilution ratios in IPA, under AM 1.5G, 100 mW cm^{-2}.

	V_{OC} (V)	J_{SC} (mA cm^{-2})	FF (%)	PCE (%)
untreated	2.102	14.32	78.79	23.72
1:20	2.169	14.28	83.88	25.98
1:10	2.171	14.44	83.13	26.06
1:5	2.172	14.51	83.29	26.25
1:2	2.173	14.59	82.35	26.11

Table S9. Photovoltaic performance parameters of untreated and poly-FPTS-treated 1.05-cm^2 POTSCs at forward and reverse scan, under the illumination of AM 1.5G, 100 mW cm^{-2}.

	V_{OC} (V)	J_{SC} (mA cm^{-2})	FF (%)	PCE (%)
Control forward	2.083	14.06	74.84	21.92
Control reverse	2.091	14.13	75.99	22.45
Poly-FPTS forward	2.164	14.26	78.11	24.10
Poly-FPTS reverse	2.159	14.25	79.69	24.52

Table S10. Photovoltaic performance parameters distribution for PCE improvements in PSCs and POTSCs after poly-FPTS treatment.

	ΔV_{OC} (%)	ΔJ_{SC} (%)	ΔFF (%)	ΔPCE (%)
PSCs	46.6	12.3	41.1	100
POTSCs	47.3	13.7	39.0	100

Table S11. Results of calculated V_{OC} loss in the PSCs without and with poly-FPTS treatment.

	ΔV_1 (mV)	ΔV_2 (mV)	ΔV_3 (mV)	$V_{OC,\,loss}$ (mV)
Control	287.8	102.6	238.5	628.9
Poly-FPTS	287.2	92.4	136.2	515.8

Supplementary Reference

1 G. Kresse and J. Hafner, *Phys. Rev. B*, 1993, **47**, 558–561.

2 P. E. Blöchl, *Phys. Rev. B*, 1994, **50**, 17953–17979.

3 J. P. Perdew, K. Burke and M. Ernzerhof, *Phys. Rev. Lett.*, 1996, **77**, 3865–3868.

4 S. Grimme, *J. Comput. Chem.*, 2006, **27**, 1787–1799.

5 S. Grimme, J. Antony, S. Ehrlich and H. Krieg, *J. Chem. Phys.*, 2010, **132**, 154104.

6 J. Moellmann and S. Grimme, *J. Phys. Chem. C*, 2014, **118**, 7615–7621.

7 T. Xu, W. Xiang, X. Ru, Z. Wang, Y. Liu, N. Li, H. Xu and S. Liu, *Adv. Mater.*, 2024, **36**, 2312237.

8 Z. Li, J. Guo, Z. Li, W. Han, G. Ren, C. Liu, L. Shen and W. Guo, *J. Mater. Chem. A*, 2020, **8**, 5629–5637.

9 Y. Wang, Y. Feng, H. Yang, S. Li, K. Zhang, Y. Feng, X. Han, T. Alshahrani, Q. An, X. Wang, H. Li, Y. Jiang and M. Yuan, *Adv. Mater.*, 2025, e07730.

10 E. A. Duijnstee, J. M. Ball, V. M. Le Corre, L. J. A. Koster, H. J. Snaith and J. Lim, *ACS Energy Lett.*, 2020, **5**, 376–384.

11 J. M. Azpiroz, E. Mosconi, J. Bisquert and F. D. Angelis, *Energy Environ. Sci.*, 2015, **8**, 2118–2127.

12 Y. Zhao, F. Ma, Z. Qu, S. Yu, T. Shen, H.-X. Deng, X. Chu, X. Peng, Y. Yuan, X. Zhang and J. You, *Science*, 2022, **377**, 531–534.

13 S. Zhang, X. Wang, Y. Wu, X. Li, T. Hou, D. Li, W. Chen, J. Li, R. Lv, Y. Zhang, Z. Xiao, T. Chen, S. Chen, Z. Fang, S. (Frank) Liu and S. Yang, *Angew. Chem. Int. Ed.*, 2025, **64**, e202508782.

14 J. Wang, J. Zhang, Y. Zhou, H. Liu, Q. Xue, X. Li, C.-C. Chueh, H.-L. Yip, Z. Zhu and A. K. Y. Jen, *Nat. Commun.*, 2020, **11**, 177.

15 X. Zhao, T. Liu, Q. C. Burlingame, T. Liu, R. Holley, G. Cheng, N. Yao, F. Gao and Y.-L. Loo, *Science*, 2022, **377**, 307–310.

16 Z. Zhang, H. Wang, T. J. Jacobsson and J. Luo, *Nat. Commun.*, 2022, **13**, 7639.

17 T. D. Siegler, W. A. Dunlap-Shohl, Y. Meng, Y. Yang, W. F. Kau, P. P. Sunkari, C. E. Tsai, Z. J. Armstrong, Y.-C. Chen, D. A. C. Beck, M. Meilă and H. W. Hillhouse, *J. Am. Chem. Soc.*, 2022, **144**, 5552–5561.

18 C. Eames, J. M. Frost, P. R. F. Barnes, B. C. O'Regan, A. Walsh and M. S. Islam, *Nat. Commun.*, 2015, **6**, 7497.

19 J. Zhang, L. Wang, C. Jiang, B. Cheng, T. Chen and J. Yu, *Adv. Sci.*, 2021, **8**, 2102648.